

## 1    **Origin and segregation of the human germline**

2  
3    Aracely Castillo-Venzor<sup>1,2,3,4,#,\*</sup>, Christopher A. Penfold<sup>1,2,3,4,#</sup>, Michael D. Morgan<sup>7,8,#</sup>, Walfred W. C.  
4    Tang<sup>1,3,4</sup>, Toshihiro Kobayashi<sup>5,6</sup>, Frederick C. K. Wong<sup>1,3,4</sup>, Sophie Bergmann<sup>2,3,4</sup>, Erin Slatery<sup>2,3,4</sup>,  
5    Thorsten E. Boroviak<sup>2,3,4</sup>, John C. Marioni<sup>7,8,9</sup> and M. Azim Surani<sup>1,2,3,4,\*</sup>

6  
7    1 Wellcome Trust/Cancer Research UK Gurdon Institute, Henry Wellcome Building of Cancer and  
8    Developmental Biology, Cambridge, CB2 1QN, UK

9    2 Wellcome - MRC Cambridge Stem Cell Institute, Jeffrey Cheah Biomedical Centre, Puddicombe  
10   Way, Cambridge Biomedical Campus, Cambridge, CB2 0AW, UK

11   3 Physiology, Development and Neuroscience Department, University of Cambridge, Cambridge, CB2  
12   3EL, UK

13   4 Centre for Trophoblast Research, University of Cambridge, Downing Site, Cambridge CB2 3EG,  
14   United Kingdom

15   5 Division of Mammalian Embryology, Center for Stem Cell Biology and Regenerative Medicine,  
16   The Institute of Medical Science, The University of Tokyo, Minato-ku, Tokyo 108-8639, Japan

17   6 Center for Genetic Analysis of Behavior, National Institute for Physiological Sciences, Okazaki, Aichi  
18   444-8787, Japan

19   7 Cancer Research UK Cambridge Institute, University of Cambridge, Li Ka Shing Centre,  
20   Robinson Way, Cambridge, CB2 0RE, United Kingdom

21   8 European Molecular Biology Laboratory, European Bioinformatics Institute, Wellcome Genome  
22   Campus, Hinxton, Cambridgeshire, CB10 1SD, United Kingdom

23   9 Wellcome Sanger Institute, Wellcome Genome Campus, Hinxton, Cambridgeshire, CB10 1RQ,  
24   United Kingdom

25   #These authors contributed equally

26   \*Correspondence to [araa.venzor@gmail.com](mailto:araa.venzor@gmail.com) (A.C.V) and [\(M.A.S\)](mailto:a.surani@gurdon.cam.ac.uk)

28 **Abstract**

29

30 Human germline-soma segregation occurs during weeks 2-3 in gastrulating embryos. While direct  
31 studies are hindered, here we investigate the dynamics of human primordial germ cell (PGCs)  
32 specification using in vitro models with temporally resolved single-cell transcriptomics and in-depth  
33 characterisation to in vivo datasets from human and non-human primates, including a 3D marmoset  
34 reference atlas. We elucidate the molecular signature for the transient gain of competence for germ cell  
35 fate during peri-implantation epiblast development. Further, we show that both the PGCs and amnion  
36 arise from transcriptionally similar TFAP2A positive progenitors at the posterior end of the embryo.  
37 Notably, genetic loss of function experiments show that TFAP2A is crucial for initiating the PGC fate  
38 without detectably affecting the amnion, and its subsequently replaced by TFAP2C as an essential  
39 component of the genetic network for PGC fate. Accordingly, amniotic cells continue to emerge from  
40 the progenitors in the posterior epiblast, but importantly, this is also a source of nascent PGCs.

41

42 **Introduction**

43

44 Human primordial germ cells (PGCs) are among the first lineages to emerge in the developing  
45 gastrulating peri-implantation embryo at weeks (Wks) 2-3, eventually developing into sperm or eggs.  
46 The parental gametes generate the totipotent state at fertilisation and transmit genetic and epigenetic  
47 information necessary for development.

48

49 The specification of PGCs is linked with the initiation of the unique germ cell transcriptomic and  
50 epigenetic program. Aberrant specification and development of germ cells can lead to sterility, germ-  
51 cell-derived cancers, and other human diseases with long term consequences across generations. Ethical  
52 and technical reasons restrict direct studies on nascent human PGCs, necessitating in vitro models,  
53 which are, however, experimentally tractable for mechanistic insights (Hirate *et al.*, 2013; Irie *et al.*,  
54 2015; Sasaki *et al.*, 2015; Tang *et al.*, 2016; Kobayashi *et al.*, 2017; Irie, Sybirna and Surani, 2018).  
55 Due to the in vitro nature of these models, comprehensive comparisons with rare human embryos and  
56 animal proxies, including in vivo development of non-human primates such as marmosets can be  
57 significantly informative for germline biology.

58

59 The induction of PGC-competent cells from cultured pluripotent stem cells (PSCs) is possible using  
60 self-renewing or transient pre-mesendoderm (PreME) populations (Irie *et al.*, 2015; Sasaki *et al.*, 2015;  
61 Kobayashi *et al.*, 2017). The timing and regulation of the transient state of competence for PGC-fate in  
62 human embryos are not yet fully defined but likely determine the number of founder PGCs in vivo. If  
63 aggregated into 3D embryoid bodies, these competent cells give rise to 10 - 40% PGC-like cells

64 (PGCLCs) in response to BMP and other cytokines (Irie *et al.*, 2015; Sasaki *et al.*, 2015; Kobayashi *et*  
65 *al.*, 2017). The remaining cells adopt somatic fates, but their relationship with the emerging PGCLCs  
66 remains unclear (Irie *et al.*, 2015; Sasaki *et al.*, 2015; Kobayashi *et al.*, 2017). Defining the  
67 characteristics of the somatic lineages in embryoid bodies may help identify soma-PGC interactions  
68 and reveal the context of how PGCs form in experimental models concerning the lineages in the embryo.  
69

70 In vitro models identified *SOX17*, *PRDM1*, and *TFAP2C* as the core regulators of human PGC fate (Irie  
71 *et al.*, 2015; Kobayashi *et al.*, 2017; Kojima *et al.*, 2017; Tang *et al.*, 2022). This tripartite network for  
72 PGC fate has also been observed in vivo in other species that develop as a bilaminar disc, including  
73 cynomolgus, marmoset, rabbit, and pig (Sasaki *et al.*, 2016; Sybirna, Wong and Surani, 2019; Alberio,  
74 Kobayashi and Surani, 2021; Kobayashi *et al.*, 2021; Zhu *et al.*, 2021; Bergmann *et al.*, 2022).  
75

76 On the other hand, *Sox17* is not a critical regulator of PGC specification in rodents where the embryos  
77 develop as egg cylinders (Kanai-Azuma *et al.*, 2002). Notably, when *SOX17* is the critical regulator for  
78 PGC specification as in humans and non-human primates, there is concomitant repression of SOX2, but  
79 not in mice, where *Sox2* has a crucial role in PGC development (Campolo *et al.*, 2013).  
80

81 The site of human PGC specification remains unclear. In cynomolgus and marmosets, PGCs are first  
82 observed in the amnion prior to gastrulation (Sasaki *et al.*, 2016; Bergmann *et al.*, 2022). At later stages,  
83 PGCs are detected in the posterior epiblast, with the possibility of a dual origin (Sasaki *et al.*, 2016;  
84 Kobayashi *et al.*, 2017; Kobayashi and Surani, 2018). Note that in humans and non-human primates,  
85 the nascent amnion is among the first lineages to form from the epiblast (Bergmann *et al.*, no date;  
86 Xiang *et al.*, 2019). In some non-primate embryos, including bilaminar disc forming species such as  
87 rabbit and pig, PGC specification precedes amnion development (Alberio, Kobayashi and Surani, 2021;  
88 Kobayashi *et al.*, 2021; Zhu *et al.*, 2021). In the pig, at least, PGCs arise from pre-primitive streak (PS)  
89 and early-PS stage competent epiblast (Kobayashi *et al.*, 2017), and in a rare Wk3 (Carnegie stage 7)  
90 human embryo, PGCs are associated with the primitive streak (Tyser *et al.*, 2021). Here we used our  
91 PSC-based model for PGC specification (Irie *et al.*, 2015; Kobayashi *et al.*, 2017) in conjunction with  
92 highly resolved single-cell transcriptome sequencing and integrative analysis with existing human and  
93 primate datasets to document the nature of the somatic components of the models and provide the  
94 context for PGCLC specification. Notably, we identified *TFAP2A*, considered an amnion marker  
95 (Shao, Taniguchi, Gurdziel, *et al.*, 2017; Shao, Taniguchi, Townshend, *et al.*, 2017), as an essential and  
96 thus far the earliest regulator of PGC fate. Loss of *TFAP2A* leads to an almost complete abrogation of  
97 PGCLCs, in favour of a population of cells displaying SOX2 expression but no significant effect on  
98 somatic lineages. The observations also provide insights into the likely origin of human PGCs.  
99

101 **Results**

102

103 **A highly resolved transcriptional characterisation of PGC specification in embryoid  
104 bodies**

105

106 Human pluripotent stem cells (PSCs) in a primed state represent non-gastrulating postimplantation  
107 epiblast cells (Yu *et al.*, 2021) with a low competence for PGCLC fate (<5%) (Irie *et al.*, 2015). PSCs  
108 can, however, acquire competence for PGC fate as self-renewing populations in media containing four  
109 inhibitors (henceforth called 4i conditions) (Gafni *et al.*, 2013; Irie *et al.*, 2015). Secondly, in response  
110 to WNT and Activin signalling, PSC can transiently acquire competence for PGC-fate at 12h, known  
111 as pre-mesendodermal cells (henceforth called Pre-ME) (Kobayashi *et al.*, 2017). Pre-ME progress to  
112 mesendoderm (ME) fate at 24h when they lose competence for PGCLC specification and instead gain  
113 competence for definitive endoderm (DE; 60-80%) and mesoderm fates (Fig. 1a).

114

115 The efficiency of PGCLC induction ranges from ~10-40% of cells in the embryoid body (EB),  
116 depending on the cell line (Chen *et al.*, 2017); the remaining non-PGCLCs cells acquire somatic fates.  
117 Using our in vitro model (Kobayashi *et al.*, 2017), we elucidate the transcriptional dynamics as the Pre-  
118 ME cells undergo specification to PGCLCs in response to BMP. To discern the changes in  
119 transcriptional states, we analysed the embryoid body at the resolution of single cells using 10X  
120 Genomics single-cell RNA-sequencing. We sampled EBs over a highly-resolve time series between  
121 12h–96h post-induction with additional comparative samples of conventional PSCs, PGC-competent  
122 populations (4i and PreME), DE and ME populations, and Wk7 human gonadal PGCs for in vivo  
123 reference (Fig. 1a).

124

125 We first sought to establish the identity of detectable lineages using droplet single cell RNA sequencing  
126 in the embryoid bodies, which fell into 15 main clusters (Supplementary Fig. 1a). Pseudo-bulk  
127 correlation showed a high degree of correlation between these clusters and amnion-like cells (AMLC),  
128 primordial germ-cell like cells (PGCLCs), or mesoderm-like cells (MELCs) (Zheng *et al.*, 2019)  
129 (Supplementary Fig. 1b). Pseudo-bulk comparison with a human in vitro embryo culture (Xiang *et al.*,  
130 2019) and the in vivo CS7 human gastrula (Tyser *et al.*, 2021) corroborates these observations, showing  
131 a higher degree of correlation between EBs and embryonic disc or amnion but a substantially reduced  
132 correlation with other extraembryonic-tissues and pre-implantation lineages (Supplementary Fig. 1c),  
133 and a comparatively low correlation with human syncytiotrophoblast (SCT) and extravillous  
134 trophoblast (EVT) (Vento-Tormo *et al.*, 2018). Together these results suggest that in response to BMP,  
135 EBs progress to lineages of the peri-gastrulation embryo but not the extraembryonic tissues except for  
136 the amnion.

137  
138 We aligned our data to a comprehensive range of existing embryonic datasets to refine cell annotations  
139 and create a human primate gastrulation and PGC atlas (Fig. 1b). We included embryonic and amniotic  
140 lineages from human and cynomolgus in vitro cultured embryos (Ma *et al.*, 2019; Xiang *et al.*, 2019;  
141 Zhou *et al.*, 2019), in vivo human and marmoset gastrula (Bergmann *et al.*, no date; Tyser *et al.*, 2021),  
142 and human gonadal primordial germ cells (Guo *et al.*, 2015; Li *et al.*, 2017). We also include three in  
143 vitro models of human PGCLC induction based on the microfluidic amnion model (Zheng *et al.*, 2019),  
144 micropatterned gastruloids (Minn *et al.*, 2020) and embryoid bodies from two other cell lines(Chen *et*  
145 *al.*, 2019) (Supplementary table 1). We show a representation of our aligned dataset as a 2D UMAP  
146 projection in Fig. 1c, with cells coloured by sampling time. For comparison, we also provide aligned  
147 samples from the human gastrula dataset (Fig. 1d), with the remaining datasets shown in Supplementary  
148 Fig. 1d-1j. Clustering across all the datasets grouped cells into approximately 30 clusters, with the key  
149 clusters visualised for our data in Fig. 1e. Initial assessment suggests a low number of doublets  
150 throughout (Supplementary Fig. 1k).

151  
152 A heatmap of gene expression of relevant lineage markers confirms the presence of a primitive streak-  
153 like population (cluster 1), as well as mesoderm-like cells (MELCs) (cluster 2-3), definitive endoderm-  
154 like cells (DELCs) (cluster 11), amnion-like cells (AMLCs) (cluster 4, 7-10), and PGC-like cells  
155 (PGCLCs) (cluster 5-6) within the EBs (Fig. 1f). We show key differentially expressed transcription  
156 factors during the formation of individual cell types in Supplementary Fig. 2. To visualise expression  
157 heterogeneity, we depict gene expression of six key lineage markers that, in combination, can be used  
158 to identify the cell fates in the EB (Fig. 1g); these findings were also confirmed at the protein level by  
159 immunofluorescence (IF) staining (Fig. 1h). Notably, our detailed integrated roadmap and  
160 characterisation show that at early stages, embryoid bodies contain subpopulations with molecular  
161 signatures similar to the PS, with cells at later time points showing transcriptional profiles associated  
162 with embryonic somatic fates (mesoderm and endoderm), PGCLCs, and amnion.

163  
164 **Detection of PGC competent population**

165  
166 Currently, there is no clear indication of what constitutes a PGC-competent population. We investigate  
167 how the precursor PreME cells gain competence for PGC-fate to address this. We also analysed the  
168 PGC-competent 4i cells against the non-competent populations (PSCs and ME) (Tang *et al.*, 2022).  
169 Comparisons with existing datasets suggested that our PSCs are transcriptionally similar to other  
170 PSCs(Chen *et al.*, 2019; Zheng *et al.*, 2019; Minn *et al.*, 2020) (Supplementary Fig. 1d-f) and align with  
171 a subset of cells from in vitro cultured human embryos labelled as EmDisc (Xiang *et al.*, 2019; Zhou *et*  
172 *al.*, 2019) (Supplementary Fig. 1g-h) and in vivo postimplantation epiblast (Tyser *et al.*, 2021) (Fig. 2a-

173 b). Conversely, PreME cells cluster with pluripotent embryonic disc sample (Xiang *et al.*, 2019; Tyser  
174 *et al.*, 2021) and cells labelled as epiblast and primitive streak and mesoderm in a human CS7 gastrula  
175 (Tyser *et al.*, 2021) (Fig. 2c).

176  
177 Since the interpretation of distances in UMAP representations remains difficult (Chari, Banerjee and  
178 Pachter, 2021), we also chose to visualise cells using diffusion maps (DM) to gauge the behaviour of  
179 these precursor populations compared to non-competent PSCs, ME populations, and terminal stage  
180 PGCLCs (Fig. 2d). These populations exist as a continuum of transcriptional states extending from  
181 PSCs to ME, and diffusion components 2 (DC2) and DC3 with PGCLCs extending out along DC1 (Fig.  
182 2e).

183  
184 Visualisation of the fraction of cell types in each subcluster identified a PSC-dominant (subcluster 1)  
185 and a ME-dominant subpopulation (subcluster 22), with three other subpopulations (subclusters 3, 14,  
186 and 19) comprised primarily of PGC-competent populations (4i and PreME) (Fig. 2f, Supplementary  
187 Fig. 3a). Pairwise differential expression analyses of PreME cells in (competent) subcluster 3 and PSCs  
188 in (non-competent) subcluster 1 identified several likely regulators of competence, including *EOMES*,  
189 which has an identified role in PGC-competence (Chen *et al.*, 2017; Kojima *et al.*, 2021), and  
190 mesodermal markers *SP5* and *MIXL1* (Fig. 2g). Additional pairwise comparison of the other competent-  
191 enriched subpopulations, e.g., subclusters 14 and 19, against cluster 1 identified similar markers,  
192 including *OTX2*, *SOX11*, *TERF1*, *TCF7L1*, *SALL2*, *LIN28A* and *TET1* (Supplementary Fig. 3b-f).  
193 Comparison of competent clusters against cluster 22 showed further upregulation of mesoderm related  
194 genes, *MIXL1*, *GATA6*, *GSC*, *MESP1*, *ZIC2*, *EOMES* in ME-dominated cluster and concomitant  
195 reduction of pluripotency factor expression (*SOX2*, *SOX3*, *NANOG*) and *MYC* in PGC-competent  
196 cluster (subcluster 3, 14, 19).

197  
198 Since competent subclusters 3, 14 and 19 showed similar marker expression (Supplementary Fig. 3b-  
199 f), we focused on subcluster 3 for simplicity (Fig. 2f). The signalling dynamics of competence gain and  
200 loss were examined by expressing key genes between clusters representing PGC-competent and non-  
201 competent cells (Fig. 2f). We observed a progressive activation of NODAL and WNT signalling  
202 together with the expression of BMP inhibitors, with the highest levels shown in the ME-dominated  
203 subcluster (subcluster 22). BMP is the inductive signal for PGC-fate, and accordingly, the PGC-  
204 competent subcluster (subcluster 3) shows a reduced expression of BMP inhibitors *CER1* ( $p < 2.17e^{-19}$ )  
205 compared to the non-competent subcluster 22. Furthermore, we observed upregulation of *NANOG* ( $p <$   
206  $9.26e^{-48}/1.62e^{-6}$ ) and concomitant downregulation of *OTX2* ( $p < 6.48e^{-10}/0.045$ ) in subcluster 3  
207 compared to non-competent clusters 1 and 22 respectively. Notably, *OTX2* negatively regulates PGCLC  
208 competence in mice (Zhang *et al.*, 2018) and we recently found that *OTX2* has a similar function in the  
209 human germline (Tang *et al.*, 2022).

210  
211 Together these analyses have identified molecular signatures that may underlie the transition from  
212 primed pluripotency to a competent state for PGC fate.

213  
214 **Specification of PGCLCs in EBs represents a primitive-streak-like stage**

215  
216 Based on the expression of marker genes, EBs first transition through a primitive-streak-like stage  
217 before diversifying into mesoderm-like (MELC), definitive-endoderm-like (DELC), and primordial  
218 germ cell-like states, with the additional formation of amnion-like cells but with a notable lack of neural  
219 ectoderm populations (Supplementary Fig. 2e). Strikingly, these are lineages expected to arise at the  
220 posterior region of the developing embryo around the time of gastrulation.

221  
222 To test this hypothesis further, we sought to map cells found in vitro to existing spatial transcriptomics  
223 datasets. Although spatially resolved human gastruloid datasets exist (Moris *et al.*, 2020), these models  
224 capture the onset of somitogenesis (CS9) and are therefore more developmentally advanced than our  
225 model, which aligns well with data from CS5-7 embryos relevant to the emergence of PGCLCs. In this  
226 regard, we note recent comprehensive spatially resolved transcriptional datasets of marmoset embryos  
227 at CS5 and CS6 (Bergmann *et al.*, 2022), where the peri-implantation development strongly resembles  
228 that of human embryo development at the morphological and transcriptional level (Bergmann *et al.*,  
229 2022), including conserved expression of *SOX17*, *PRDM1*, *TFAP2C* and *NANOS3* in PGCs.  
230 Notwithstanding the differences in human and marmoset development timing, archival embryo  
231 collections allow consistent staging between species based upon Carnegie staging (Strachan, Lindsay  
232 and Wilson, 1997; O’Rahilly and Müller, 2010).

233  
234 To evaluate possible anterior-posterior bias, we mapped cells from our in vitro model to an existing 3D  
235 spatially resolved depiction of a CS6 marmoset embryo in which laser capture microdissection was  
236 used to generate a 3D spatially resolved transcriptome (see Materials and Methods). Together, they  
237 capture the critical cell types for comparison (Fig. 3a) with gene expression patterns of critical markers  
238 shown in Fig. 3b. We found that pluripotent stem cell populations mapped best to the anterior  
239 compartment (Fig. 3c), in agreement with earlier studies (Tyser *et al.*, 2021; Bergmann *et al.*, 2022),  
240 although we could not rule out that these cells might have a better mapping to earlier stages, e.g., CS4  
241 bilaminar disc embryo since no data for this stage is available. We found that the PreME population  
242 shifted towards the posterior end of the embryo, with amnion-like cells primarily mapping to the  
243 posterior amnion (Fig. 3c). The basal cluster, which represents the 12h embryoid body mapped to the  
244 posterior end of the embryonic disc to a region expression *TBX7* and other primitive streak markers.  
245 Other cell lineages, including PGCLCs, showed an even stronger bias to the posterior end of the embryo,

246 with PGCLC mapping to a distinct *NANOS3*-expressing region between the posterior-most embryonic  
247 disc and amnion (Fig. 3a). Together, these results provide further evidence that our model represents  
248 the development of the posterior end of the embryo during gastrulation and suggests ongoing  
249 specification of both amnion and primordial germ cells.

250

## 251 **Highly resolved time series reveal dynamics of cell trajectories**

252

253 Having established the identity and spatial correspondence of key lineages, we next investigated the  
254 dynamics of individual cell fate decisions within the EB. We performed a label transfer from the human  
255 CS7 gastrula dataset (Tyser *et al.*, 2021) to our data and separated EBs by collection time to visualise  
256 the emergence of cell types (Fig. 4a). Twelve hours after inductive BMP cues, cells aligned primarily  
257 to the primitive streak (PS) with a limited pool of epiblast-like cells. Primitive streak-like cells (PSLCs)  
258 persisted in limited numbers until ~24-32h, with sustained expression of *NODAL* (Supplementary Fig.  
259 4). Nascent and emergent mesoderm-like cells (denoted nMELC, eMELC) appeared as early as 12h,  
260 becoming more pronounced by 18h, with these lineages roughly corresponding to cluster 2. The earliest  
261 PGCLCs arose around the 18h mark, with amnion-like cells and definitive endoderm-like cells around  
262 24h.

263

264 We visualised the segregation of early mesoderm from precursors with primitive-streak-like identity  
265 using a diffusion map (Fig. 4b). Cells not committed to mesoderm-fate are instead predominately  
266 directed towards PGCLC or AMLC. Both UMAP and DM representations suggest that PGCLCs and  
267 AMLCs stem from highly similar progenitor cells (Fig. 4b). Interestingly, there remains some  
268 association between the PGCLC and AMLC branches until around 48h, with a number of cells falling  
269 between the two main branches. Visualisation of the PGCLC branch alongside samples from the CS7  
270 human gastrula shows an overlap between the gastrula samples and our Wk7 *in vivo* PGCs and late *in*  
271 *vitro* PGCLCs (Fig. 4c). It is also worth noting that four other cells, initially labelled as PS in the human  
272 gastrula dataset, were also found to align to early PGCLCs and were reannotated accordingly. Together  
273 these observations strongly suggest that the CS7 gastrula contains samples of PGCs at different stages  
274 of specification and that our *in vitro* model captures the dynamics of this developmental trajectory at a  
275 much finer resolution. Cross comparison of CS7 PGCs with PGCLCs from various other *in vitro* models  
276 confirms a robust and conserved program of PGCLC-specification centred around the  
277 *SOX17/TFAP2C/PRDM1* network with consistent up-regulation of *TFAP2A* and other genes  
278 (Supplementary Fig. 5).

279

280 We quantified the dynamics of individual bifurcations by inferring lineage trajectories with  
281 Waddington-OT (Schiebinger *et al.*, 2019), an optimal transport-based approach that allowed us to infer

282 progenitor-progeny relationships between groups of cells statistically. By integrating these results with  
283 reduced dimensional representations of our time-course data, such as UMAP, DM, or PCA, we sought  
284 to identify the most likely earliest progenitors of PGC specification in our data. Using the ancestor-  
285 progeny relationships computed by WOT we inferred the broader lineages by first constructing a sparse  
286 network of clusters (Supplementary Fig. 6a,b) which were further grouped using a community-detection  
287 algorithm (see Methods). We assigned the inferred lineage identities to the single cells in these groups  
288 using broad marker gene expression patterns. As an initial check, we overlaid these WOT-inferred  
289 lineages onto our UMAP in Supplementary Fig. 6c, which demonstrated a good agreement with our  
290 earlier annotation-based lineage assignments with a high degree of correlation to our earlier cluster and  
291 marker-based annotations (Supplementary Fig. 6d). Using Waddington-OT inference, most terminal  
292 cell fates were effectively traced to 24h, with some cell groups traced to earlier stages.

293

294 Early mesoderm populations progressed from a PS-like state through a nascent-mesoderm-like state  
295 (nMELC) expressing *MESP1/2* and *T* to an emergent mesoderm-like state (eMELC), representing the  
296 highest levels of *MESP1/2* and downregulation of *T* (Supplementary Fig. 6e-f). Between 24 to 32h, a  
297 *PDGFRA* positive population emerged, aligned to advanced mesoderm of the human gastrula (denoted  
298 advanced mesoderm-like cells; aMELC), concomitant with the gradual loss of nMLC and eMLC  
299 subpopulations. By ordering gene expression along a diffusion pseudotime analysis, we observed the  
300 late up-regulation of several advanced mesoderm markers, *HAND1*, *SNAI2* and *GATA6* (Supplementary  
301 Fig. 6e-g). As the earliest specified fate, nascent and emergent mesoderm cells express several genes  
302 that may influence the balance of fates within the embryoid body, including *BMP4*, *WNT5A*, and *CER1*,  
303 and extra-cellular matrix genes (see e.g., Supplementary Fig. 4).

304

305 From 24h to 32h, a limited pool of *SOX17*-positive endoderm-like cells bifurcated from the PS-like  
306 subpopulation and showed sustained *NODAL* expression with subsequent upregulation of endoderm  
307 markers *FOXA1/2* (Supplementary Fig. 6h,i). Although the number of cells in this population appeared  
308 to be fewer than that of other cell lineages, it was nevertheless a conserved feature across in vitro  
309 models.

310

311 Around the 18-hour mark, the earliest PGCLCs bifurcated from a progenitor population with strong up-  
312 regulation of *SOX17*, *TFAP2C*, and *PRDM1* (see Supplementary Fig. 2g-h) and subsequent expression  
313 of *NANOS3*. PGCLCs also showed up-regulation of *WNT2* with early PGCLCs expressing *NODAL*  
314 (Supplementary Fig. 4).

315

316 Indeed, a comparison of PGCLC-precursor cells in high and low PGC-competence cell lines (Chen *et*  
317 *al.*, 2019) revealed *NODAL* to be differentially expressed, consistent with a recently observed role for  
318 *NODAL* in PGCLC specification (Jo *et al.*, 2021). Slightly later, at 24h, an AMLC branch also became

319 evident, expressing *TFAP2A* and, at later time points, *ISL1*, a LIM/homeodomain transcription factor  
320 protein recently identified as an amnion marker (Guo *et al.*, 2020; Yang *et al.*, 2021) (Supplementary  
321 Fig. 2c-d). This AMLC branch shows an expression of *WNT6* (Supplementary Fig. 4). We identified  
322 differentially expressed genes along the separate AMLC and PGCLC lineages using the diffusion  
323 pseudotime ordering of single cells (Fig. 4d; see Supplementary Materials). Within these pseudotime  
324 trajectories, we observed that both AMLC and PGCLC showed early coordinated expression of  
325 *EOMES*, *MIXL1* and *ZIC*, together with rapid downregulation of *SOX2*. Moreover, we observed late  
326 expression of *VTCN1*, *GATA3*, *GATA2*, *ISL1* and *HAND1* in AMLCs, while the PGCLC trajectory  
327 showed late expression of PGC markers *SOX17*, *PRDM1*, *TFAP2C*, *SOX15*, *KLF4*, *LIN28*, and  
328 *POU5F1*. Fig. 4e shows the divergent expression patterns of crucial TFs over pseudotime to trace their  
329 rise and fall to AMLC versus PGCLC trajectories. We note an initial up-regulation of *SOX17* in AMLC  
330 and PGCLCs that is transient in AMLC but sustained in PGCLCs. Surprisingly, *TFAP2A*, which is  
331 generally considered a trophoblast or amnion marker (Krendl *et al.*, 2017; Zheng *et al.*, 2019; Minn *et*  
332 *al.*, 2020), precedes *SOX17* expression and is transiently co-expressed with *SOX17* in the PGCLC  
333 trajectory. While AMLCs maintain *TFAP2A* expression, there is downregulation in PGCLCs, which  
334 was confirmed by immunofluorescence staining at the protein level (Fig. 4f). Staining of EBs for  
335 *TFAP2A* and *SOX17* confirmed their co-expression at early time points, whereas, in the 96h EB,  
336 *TFAP2A* expression is exclusive to AMLC and *SOX17* to PGCLCs and DELCs. These results, taken  
337 together, highlight the complex dynamics of PGCLC specification within our model system and identify  
338 several putative markers of specification. The most interesting was the early and transient expression  
339 of *TFAP2A* in PGCLCs. *TFAP2A* is an early BMP response gene that shares the TF binding site with  
340 *TFAP2C* (Krendl *et al.*, 2017). Given that we previously found TFAP2 motifs around PGC-related  
341 genes (Tang *et al.*, 2022), and that the TFAP2 family can play complementary roles, it is interesting to  
342 see if *TFAP2A* plays a role in PGCLC specification before the onset of *TFAP2C* expression.  
343

#### 344 **TFAP2A is the most upstream crucial regulator of PGC specification**

345  
346 To determine whether the transient *TFAP2A* expression has a role in PGC fate, we induced PGCLCs  
347 via PreME states using PSCs with a knockout mutation in *TFAP2A* and compared the outcome with the  
348 parental PSC line (Krendl *et al.*, 2017) (Fig. 5a). We observed a reduction in PGCLCs in *TFAP2A*  
349 mutant cells compared to parental controls by FACS using antibodies for PGC-surface markers PDPN  
350 and AP (2.78% vs 9.28%) (Fig. 5b). Quantification of four independent experiments showed a  
351 consistent and statistically significant reduction in PGCLC specification in *TFAP2A* KO EBs (Fig. 5c)  
352 confirmed by immunofluorescence staining of d4 EBs generated from *TFAP2A* knockout cells,  
353 compared to parental control (Fig. 5d).  
354

355 To characterise the phenotype due to *TFAP2A* loss of function further, we generated 10X scRNA-seq  
356 datasets for two-time points: 18h, just before the diversification of distinct lineages in embryoid bodies,  
357 and at 96h, when terminal cell fates have been established. We integrated these time points with our  
358 existing EB dataset containing all cell types for reference using Seurat. For this alignment, we generated  
359 a new clustering visualised on a UMAP in Fig. 5e.

360

361 Embryoid bodies in parental lines showed the precise formation of a MELC expressing *PDGFRA*,  
362 amnion expressing *VTCN1*, and PGCLCs expressing *NANOS3* by 96h (Fig. 5e), suggesting conserved  
363 terminal behaviour with previous lines. While there were no detectable DELCs in either the parental or  
364 *TFAP2A* KO line by scRNA-seq, likely due to their limited cell numbers, immunofluorescence analysis  
365 shows that rare *SOX17*, *FOXA2* double-positive cells were present in the EB (Supplementary Fig. 7a).  
366 On the other hand, in EBs with *TFAP2A* KO cells, PGCLC lineages were virtually absent (Fig. 5E,  
367 Supplementary Fig. 7a-b), but aMELC and AMLC populations were present. While the *TFAP2A* KO  
368 appeared to lack PGCLCs, we observed a new subpopulation of cells at 96h clustered alongside  
369 pluripotent cells (Fig. 5e). This population, absent in the parental line and rare at the 18h mark in the  
370 KO line, showed expression of *SOX2* and other pluripotency markers (hereafter referred to as *SOX2+d4*  
371 cells; Supplementary Fig. 7c).

372

373 To help establish the authenticity of the other fates, we generated a cross-correlation heatmap  
374 (Supplementary Fig. 7d). The *SOX2+d4* cluster is most similar to PSCs in the reference population.  
375 AMLCs in the KO cluster were highly similar to AMLCs in the parental line and the reference line,  
376 with MELCs also showing consistency across all cell lines. Together these observations suggest no  
377 significant effect of *TFAP2A* loss of function for MELCs or AMLCs specification.  
378 Immunofluorescence analysis confirmed the presence of AMLCs (*GATA3+* *HAND1+*), MELCs  
379 (*HAND1+*) (Supplementary Fig. 7e), and DELC cells (*SOX17+*, *FOXA2+*) in *TFAP2A* KO in  
380 *TFAP2A* KO EBs but with a minimal number of PGCLCs (*SOX17+*, *OCT4+*) (Supplementary Fig.  
381 7a), confirming that *TFAP2A* had no significant effect on the other fates of the EB. We, therefore,  
382 focused on PGCLCs and the *SOX2+* population.

383

384 Differential expression analysis of the *SOX2+d4* population compared to parental-line PGCLCs  
385 showed that the *SOX2+d4* cells expressed pluripotency and neural-plate factors, *ZIC2*, *ZIC5*, *SOX11*,  
386 *OTX2*, while PGCLCs showed expression of germ cell markers *SOX17*, *PRDM1*, *SOX15*, *ARID5B*,  
387 *TFCP2L1* and *VENTX* (Fig. 5g). We found upregulation of naïve markers of pluripotency and neuronal  
388 lineage-associated genes in the *SOX2+d4* population compared to PSCs in the reference atlas; markers  
389 included *PRDM14*, *KLF4*, *KLF6*, and *TFAP2C*, and neuro-related genes *ZIC2*, *ZNF292*, *FOXN3*,  
390 *POU3F1*, *SOX11*, *SOX4*, *ZIC5*, and *SALL3* (Supplementary Fig. 7f).

391

392 To validate our findings at the protein level, we performed immunofluorescence staining at d4 EBs and  
393 found expression of *SOX2* in TFAP2A KO cells even after four days of cytokine exposure. There was  
394 a rapid downregulation of *SOX2* upon BMP exposure (Supplementary Fig. 7c) in WT cells, which is  
395 critical for efficient PGCLC specification(Lin *et al.*, 2014). *SOX2*+d4 cells also showed co-expression  
396 of *OCT4* and *NANOG* (Fig. 5h).

397  
398 We investigated if TFAP2A could potentially target *SOX2* for downregulation based on these results.  
399 For this, we generated a stable dox-inducible TFAP2A PSCs line. Upon doxycycline induction of  
400 *TFAP2A* in PSCs cultured in E8 medium by dox for two days (Fig. 5i), we observed a substantial  
401 reduction in *SOX2* levels after TFAP2A overexpression by immunofluorescence (Fig. 5j). *POU5F1*  
402 was also slightly reduced. Together, our results suggest that TFAP2A is a regulator of PGCLC fate and  
403 may participate in the downregulation of *SOX2* and other targets impeding PGCLC specification.

404  
405 **Discussion**

406  
407 In vitro models have been of vital importance for unravelling the transcriptional network responsible  
408 for human germ cell competence and specification (Teo *et al.*, 2011; Irie *et al.*, 2015; Sasaki *et al.*,  
409 2015; Chen *et al.*, 2017; Kobayashi *et al.*, 2017; Kojima *et al.*, 2017, 2021; Pierson Smela *et al.*, 2019;  
410 Sybirna *et al.*, 2020). In this study, we characterise in vitro models for the derivation of PGCLCs from  
411 PSCs by highly resolved single-cell transcriptomics and comprehensive comparison to in vivo  
412 references in human, non-human primates, and other in vitro models of gastrulation.

413  
414 Notably, we found that PGC competent PreME cells exist transiently within a continuum of states  
415 extending from PSCs to mesendoderm (ME). Our analysis showed that clusters enriched for PGC-  
416 competent populations present a particular signalling signature, characterised by active Nodal and WNT  
417 signalling. There is low expression of BMP inhibitors (*BAMBI* and *CER1*) in competent cells compared  
418 to the ME-dominated cluster with the highest levels in non-competent cluster 22, which likely impedes  
419 PGC specification. *BAMBI* is a direct target of WNT signalling (Sekiya *et al.*, 2004), while activation  
420 of *CER1* occurs via both WNT and Nodal signalling (Katoh and Katoh, 2006; Martyn, Brivanlou and  
421 Siggia, 2019). PGCLC-competent clusters also show transient downregulation of *OTX2* and higher  
422 levels of *NANOG* compared to non-competent clusters, which we recently found is conducive to  
423 transition to the PGCLC state (Tang *et al.*, 2022). Concomitantly, there is an increase in the levels of  
424 *EOMES*, which has a prominent role in human PGC-competence (Chen *et al.*, 2017; Kojima *et al.*,  
425 2017), but further activation of mesoderm factors hinders PGC specification. The tight signalling axis,  
426 transcription factor levels and intrinsic heterogeneity modulating competence are consistent with a

427 relatively small number (~100-200) of founder PGCs in vivo (Saitou, Barton and Surani, 2002;  
428 Kobayashi *et al.*, 2017).

429  
430 Specification of PGCLCs in vitro occurs within a 3D aggregate that consists of a hitherto poorly  
431 characterized fraction of somatic components. Currently, PGCLCs can be induced in various 2D  
432 aggregates but more efficiently in 3D embryoids, highlighting the importance of the structure, cell-cell  
433 interactions or signalling from adjacent tissues (Minn *et al.*, 2020, 2021). Here we have shown that  
434 these somatic cells collectively represent those in the posterior region of the embryo during gastrulation.  
435 Among the somatic cell types, we note the early formation of mesoderm-like cells, which display strong  
436 expression of BMP, WNT, and ECM components that may be important for PGC-fate and potentially  
437 play a similar role to that of extraembryonic mesoderm in the embryo, and endoderm-like cells that are  
438 double positive for *FOXA2/SOX17*. Furthermore, we also observe the emergence of *ISL1/VTCN1*  
439 expressing amnion cells, providing evidence that amnion formation continues from the posterior  
440 epiblast during gastrulation, as recently suggested in a study on marmoset (Bergmann *et al.*, 2022).

441  
442 Mapping the cells to a 3D primate embryo showed that PSCs best correspond to the anterior region of  
443 the embryonic disc, while PreME cells shifted towards the posterior end. Conversely, cells within the  
444 newly formed embryoid body at 12h, which transcriptionally resemble a primitive streak, mapped best  
445 to the posterior end of the embryonic disc, with PGCLCs mapping to a *SOX17/TFAP2C/NANOS3*  
446 positive region at the boundary between the posterior-most epiblast and amnion.

447  
448 The origin of human PGCs remains unresolved due to the inaccessibility of human embryos, but  
449 bilaminar disc embryos from other species provide valuable information. In species such as the rabbit  
450 and pig, PGCs originate from the posterior epiblast, but the amnion develops later, indicating that the  
451 development of the amnion and PGCs in some cases are temporally unconnected. In humans and non-  
452 human primates, development of the amnion commences prior to PGC specification, but according to  
453 our work and by others (Bergmann *et al.*, 2022; Rostovskaya *et al.*, 2022) amniotic cells continue to  
454 emerge later from the posterior epiblast, co-incidentally with the specification of PGCs at the time of  
455 primitive streak formation. In cynomolgus monkeys, the earliest PGCs have been reported in the  
456 amnion, with the majority found later in the epiblast. One possibility is that these early PGCs may arise  
457 from intermediate cells that are en route to the amnion but are but not fully committed as squamous  
458 amniotic epithelium as observed in our data (Fig. 4c). To contribute to the founder PGC pool, PGCs  
459 arising in the amnion would need to migrate against the continuing amnion growth. We posit that at this  
460 stage of development in humans and non-human primates, amnion cells continue to be specified with  
461 nascent PGCs arising at the posterior-most end of the epiblast during the early PS stage.

462

463 In our model, AMLC and PGCLC progenitors display early expression of *TFAP2A*, a pioneer factor  
464 previously associated with the amnion (Shao, Taniguchi, Townshend, *et al.*, 2017). Whilst there is  
465 subsequent downregulation of *TFAP2A* in PGCLCs, expression is sustained in the amnion.  
466 Surprisingly, the knockout of *TFAP2A* did not have a detectable effect on AMLCs, which merits further  
467 investigation, but notably resulted in an almost complete abrogation of PGCLCs.

468

469 In PGCLCs, *TFAP2A* is rapidly replaced by the expression of *TFAP2C*, suggesting otherwise mutually  
470 exclusive expression after a brief window of co-expression. Interestingly, *TFAP2A* shares the same  
471 transcription factor binding motif as *TFAP2C* (Krendl *et al.*, 2017). *TFAP2C* is essential for PGC  
472 development (Kojima *et al.*, 2017) and acts as both an activator and a repressor during PGC  
473 specification but it is not sufficient for PGC fate in the absence of cytokines (Kobayashi *et al.*, 2017).  
474 In the PGCLC pseudotime trajectories, we saw early upregulation of *TFAP2A* (12h), followed by  
475 expression of *SOX17* and *TFAP2C* (18h), and later, activation of *PRDM1* (24-32h) by *SOX17* (Tang *et*  
476 *al.*, 2022) (Supplementary Fig. 8). In some instances, *TFAP2A* functions similarly to *TFAP2C*  
477 (Hoffman *et al.*, 2007; Li and Cornell, 2007). Our work suggests that *TFAP2A* expression is transient  
478 but essential for initiating the PGC transcriptional network, and may directly or indirectly repress *SOX2*  
479 and other factors.

480

481 *TFAP2A* KO EBs show an emergent population (*SOX2*<sup>+</sup> d4 cells) found to align to pluripotent stem  
482 cells, with the expression of the core pluripotency genes; *SOX2*, *POU5F1* and *NANOG*. Differential  
483 gene expression between PSCs and *SOX2*<sup>+</sup> d4 cells shows aberrant upregulation of naïve markers  
484 *KLF4*, *TFAP2C* and *PRDM14* and genes associated with the neuronal lineage, including *ZNF292*,  
485 *FOXN3*, *SALL3*, *ZIC2*, *POU3F1* in *SOX2*<sup>+</sup> d4 cells.

486

487 There is rapid downregulation of *SOX2* during human PGCLC-induction (Kobayashi *et al.*, 2017);  
488 indeed, sustained *SOX2* expression prevents PGCLC specification due to elevated differentiation into  
489 the neuronal lineage (Lin *et al.*, 2014), which could in part explain the expression of related neuronal  
490 markers in the *TFAP2A* mutant cells. The combinatorial role of *SOX17*-*OCT4* involved in human germ  
491 cell fate (Tang *et al.*, 2022) might benefit from a repression of *SOX2* to favour the *SOX17*-*OCT4*  
492 interaction on the compressed motif.

493

494 We provide insight into early human development with the transient emergence of the germ cell  
495 competent PreME cells in a model mimicking human gastrulation starting with PSC. Our study  
496 suggests continuing emergence of the amnion from the posterior epiblast at the time of PGC  
497 specification during early gastrulation; the amnion and PGC likely arise from highly similar progenitor  
498 exemplified by *TFAP2A* expression. The loss of function has a marked effect on PGC specification but  
499 without a detectable effect on the amnion. Accordingly, PGCs likely emerge from the posterior epiblast

500 predominantly, notwithstanding a sub-set in the early amnion (Fig. 6). Of great interest would be to test,  
501 when possible, the predictions we make by direct observations in extended cultures of developing  
502 human embryos.

503

## 504 **Material and methods**

505

### 506 **Cell culture**

507 H1 NANOS3-tdTomato PSC line was previously generated in the lab (Kobayashi et al., 2017). H9  
508 parental and TFAP2A KO cells were kindly provided by Micha Drukker (Krendl et al., 2017). All cell  
509 lines were confirmed as mycoplasma negative. PSCs were maintained on vitronectin-coated plates in  
510 Essential 8 medium (Thermo Fisher Scientific) according to the manufacturer's protocol. Cells were  
511 passaged every three to four days using 0.5 mM EDTA in PBS without breaking cell clumps.

512 For the 4i condition, undifferentiated PSC cells were maintained on irradiated mouse embryonic  
513 fibroblasts (MEFs) (GlobalStem) in 4i medium (Irie et al., 2015). 4i were passaged every three to five  
514 days using TrypLE Express (Gibco) quenching with MEF media and filtered with 50 µm cell filter  
515 (PERTEC). ROCK inhibitor (10 µM; Y-27632, Tocris Bioscience) was kept in the culture for 24 h  
516 after passaging.

517 Mesendoderm induction was performed as reported in (Kobayashi et al., 2017). PSCs were dissociated  
518 into single cells using TrypLE Express and seeded onto vitronectin coated plates at 500,000 cells per  
519 well of 6-well plate and cultured in mesendoderm (ME) induction medium for 10 to 12 hours. ME  
520 medium is based on aRB27

521 Primordial germ cells were induced as reported previously (Irie et al., 2015; Kobayashi et al., 2017).  
522 For this PreME cells were disaggregated into single cell solution using TrypLE, then 4,000 cells per  
523 well were seeded into ultra-low attachment 96-well plates (Corning Costar) in PGC induction medium.  
524 Mesendoderm, PGCLC and definitive endoderm were induced from NANOS3-tdTomato reporter  
525 PSCs as described before (Kobayashi et al., 2017) using the aRB27 basal medium, which was composed  
526 of Advanced RPMI 1640 Medium (Thermo Fisher Scientific) supplemented with 1% B27 supplement  
527 (Thermo Fisher Scientific), 0.1 mM NEAA, 100 U/ml penicillin, 0.1 mg/ml streptomycin, 2 mM L-  
528 glutamine. To induce mesendoderm, trypsinized hPSCs were seeded on vitronectin-coated dishes at  
529 200,000 cells per well in a 12-well plates and cultured in mesendoderm induction medium for 12  
530 (PreME) and 24 (ME) hours. Mesendoderm induction medium contained aRB27 medium supplemented  
531 with 100 ng/ml activin A (Department of Biochemistry, University of Cambridge), 3 µM GSK3i  
532 (Miltenyi Biotec) and 10 µM of ROCKi (Y-27632, Tocris bioscience). To induce definitive endoderm  
533 from ME, mesendoderm induction medium was replaced with definitive endoderm induction medium  
534 after washing with PBS once and cells were cultured for a further 2 days. Definitive endoderm induction  
535 medium was composed of aRB27 medium supplemented with 100 ng/ ml activin A (Department of  
536 Biochemistry) and 0.5 µM BMPi (LDN193189, Sigma).

537  
538 To induce PGCLCs, PreME cells were trypsinized into single cells and harvested into Corning Costar  
539 Ultra-Low attachment multiwell 96-well plate (Sigma) at 4,000 cells per well in hPGCLC induction  
540 medium, which composed of aRB27 medium supplemented with 500 ng/ml BMP4, 10 ng/ml human  
541 LIF (Department of Biochemistry), 100 ng/ml SCF (R&D systems), 50 ng/ml EGF (R&D Systems), 10  
542  $\mu$ M ROCKi, and 0.25% (v/v) poly-vinyl alcohol (Sigma). Cells were cultured as floating aggregate for  
543 2-4 days.

544  
545 To collect PSCs, PreME, ME, DE, PGCLCs, cells were trypsinized with 0.25% trypsin/EDTA at 37 °C  
546 for 5-15 min. DE was stained with PerCP-Cy5.5 conjugated anti-CXCR4 antibody (Biolegend). Cell  
547 suspension was subjected to FACS by SH800Z Cell Sorter (Sony) and analyzed by FlowJo software.

548  
549 **Collection of human PGCs from human embryos**

550  
551 Human embryonic tissues were used under permission from NHS Research Ethical Committee, UK  
552 (REC Number: 96/085). Human embryonic samples were collected following medical or surgical  
553 termination of pregnancy carried out at Addenbrooke's Hospital, Cambridge, UK with full consent from  
554 patients. Crown-rump length, anatomical features, including limb and digit development, was used to  
555 determine developmental stage of human embryos with reference to Carnegie staging (CS). The sex of  
556 embryos were determined by sex determination PCR as previously described (Bryja and Konečný,  
557 2003).

558  
559 Human embryonic genital ridges from individual embryos (wk7) were dissected in PBS and separated  
560 from surrounding mesonephric tissues. The embryonic tissues were dissociated with Collagenase IV  
561 (2.6 mg/ml) (Sigma, C5138) and DNase I (10 U/ml) in DMEM-F12 (Gibco) at 37°C for 15-30 minutes  
562 (depending on tissue size). Tissues were pipette up and down for five times every 10 minutes to facilitate  
563 dissociation into single cell suspension. After that, samples were diluted with 1 ml FACS medium (PBS  
564 with 3% fetal calf serum & 5 mM EDTA) and centrifuged at 500 xg for 5 minutes. Cell pellet was  
565 suspended with FACS medium and incubated with 5  $\mu$ l of Alexa Fluor 488-conjugated anti-alkaline  
566 phosphatase (BD Pharmingen, 561495) and 5  $\mu$ l of APC-conjugated anti-c-KIT (Invitrogen, CD11705)  
567 antibodies for 20 minutes at room temperature with rotation at 10 revolutions per minutes (rpm) in dark.  
568 Cell suspension was then diluted in 1 ml FACS medium and centrifuged at 500 xg for 5 minutes. After  
569 removing the supernatant, the cell pellet was resuspended in FACS medium and passed through a 35  
570  $\mu$ m cell strainer. FACS was performed with SH800Z Cell Sorter (Sony) and FACS plots were generated  
571 by FlowJo software.

572  
573 **Fluorescence-activated cell sorting (FACS)**

574  
575 PSCs, 4i, PreME and ME cells were harvested using TrypLE (GIBCO) at 37°C for 2-3 min. Embryoid  
576 bodies were collected and dissociated into single cells using Trypsin-EDTA solution 0.25% at 37°C for  
577 5 to 15 min. Dissociated cells were washed and resuspended in the FACS buffer (PBS 3% FCS). DE  
578 samples were stained with PerCP-Cy5.5 conjugated anti-CXCR4 antibody (Biolegend) for 1h on ice.  
579 Samples were washed with PBS, stained with DAPI (1:10,000) and sorted on a SONY SH800 sorter.  
580

581 Human embryonic genital ridge or mesonephros from a week 7.0 male embryo were collected in  
582 dissection medium (DMEM (Gibco), 10% FCS, 1 mM sodium pyruvate (Sigma)). Embryonic tissues  
583 were dissociated with 300 µL collagenase IV (2.6 mg/mL in DMEM-F/12) supplemented with DNaseI  
584 (10U/mL) per genital ridge and incubated for 10 minutes at 37°C with mixing by pipetting up and down.  
585 Then, cells were washed with 1 mL FACS buffer (PBS with 3% FCS and 5 mM EDTA). Resuspended  
586 with 75 µL FACS buffer and stained with 0.5 µL alexa Fluor 488-conjugated anti-alkaline phosphatase  
587 (BD Pharmingen, 561495) and 25 µL of PerCP- Cy5.5-conjugated anti-CD117 (BD Pharmingen  
588 333950) for 15 minutes at room temperature. Samples were washed with PBS and sorted on a SONY  
589 SH800 cytometer. Flow cytometry data was analysed on FlowJo v10 (FlowJo LLC).

590  
591 **Immunofluorescence**  
592  
593 Embryoid bodies (EBs) were fixed in 4% PFA for 2h at 4 °C and embedded in O.C.T. compound  
594 (Cellpath) for frozen sections. Each sample was incubated with primary antibodies for 1–2 h at room  
595 temperature or overnight at 4°C and then with fluorescent-conjugated secondary antibodies and DAPI  
596 (Sigma) for 1 h at room temperature. Samples were then imaged under a Leica SP8 upright or inverted  
597 scanning confocal microscope.

598 Cells were cultured on ibidi µ-Slide and fixed in 4% PFA for 30 minutes at 4°C. Embryoid bodies were  
599 fixed in 4% PFA for 2 hours at 4°C and embedded in OCT compound for frozen sections. The samples  
600 were incubated with primary antibodies overnight at 4°C and subsequently with fluorescence-  
601 conjugated secondary antibodies (Thermo Fisher Scientific) and DAPI for 1 hour at RT. The primary  
602 antibodies used are: anti-GFP (abcam, ab13970), anti-PRDM1 (Cell Signaling Technology, 9115), anti-  
603 SOX17 (R&D, AF1924), anti-TFAP2C (Santa Cruz Biotechnology, sc-8977), and anti-OCT4 (BD  
604 Biosciences, 611203). Samples were imaged under Leica SP8 upright or inverted scanning confocal  
605 microscope.

606  
607 **10X genomics**  
608  
609 For each stage, 5,000 cells were sorted into an eppendorf tube containing PBS with 0.04%  
610 weight/volume BSA (400 µg/mL). Samples collected are listed in table 2.6. During sorting, dead cells,

611 debris and doublets were gated out. Sorted cells were directly taken for 10x processing at Cancer  
612 Research UK, Cambridge Institute and loaded into the 10x-Genomics Chromium using the single cell  
613 3' reagents kit v2. Libraries were prepared as per the manufacturer's instructions and pooled for  
614 sequencing so that all lines would include all samples. Libraries were sequenced, aiming at a minimum  
615 coverage of 50,000 raw reads per cell, on an Illumina HiSeq 4000 (paired-end; read 1: 26 cycles; i7  
616 index: 8 cycles, i5 index: 0 cycles; read 2: 98 cycles).

617

## 618 **Bioinformatics**

619

### 620 **10X RNA sequencing processing**

621

622 Multiplexed single-cell libraries were processed using the 10X Genomics cell ranger pipeline. Reads  
623 were aligned to a reference genome (*Homo sapiens* GrCh38) using STAR (Dobin et al., 2013), and  
624 quantification of genes against an annotation reference (based on Ensembl GrCh38 v90).

625

## 626 **Analysis**

627

628 Initial analysis of our data was done using Seurat (v3.1.4) (Stuart et al., 2019). Count data was  
629 normalised and scaled using NormalizeData based on log counts per 10000 (logCP10k) and scaled  
630 using ScaleData. Clusters were generated using FindCluster with resolution of 0.1. Nearest neighbour  
631 graphs and UMAP plots were calculated using the first 20 PCs.

632

633 Heatmaps of gene expression were generated based on row-scaled values using pheatmap (v.1.0.12)  
634 with cross-correlations calculated based on Pearson's correlation and visualised using pheatmap.

635

## 636 **Integrative analysis**

637

638 Individual datasets were first curated to remove pre-implantation and extraembryonic tissues. Datasets  
639 were then integrated based on logCP10k using FindIntegrationMarkers with 5000 integration features  
640 and k.filter=50. Data was integrated based on CCA with 5000 features and using the first 20 PCs. Joint  
641 clustering was generated based on the integration-corrected gene expression matrices using the  
642 FindClusters function with complexity parameter uniformly incremented from 0.1-0.9 in steps of 0.1.  
643 For visualisation purposes we used parameter of 0.9 for the figures within the paper.

644

645 For initially establishing cell fates expression of key marker genes were plotted as a heatmap using  
646 pheatmap. To establish veracity of cell types between datasets, a scatter plot of differential expression  
647 was used with the x-axis showing logFC of a specific cluster vs a reference cell type/cluster (e.g., cluster

648 0 vs PSCs) with the y-axis showing the same comparison (cluster 0 vs PSCs) in the second dataset.  
649 Genes in the top right and bottom left quadrants represented conserved changes between the two  
650 datasets, whilst genes to the top left or bottom right represented dataset specific changes.

651  
652 As a preliminary visualisation of individual bifurcations, diffusion maps were generated for selected  
653 sets of subclusters using destiny (v2.12.0) (Angerer et al., 2016) based on integration-corrected  
654 expression matrices.

655  
656 **Differential expression analysis**

657  
658 Unless otherwise indicated, differential expression between two groups was done in Seurat using MAST  
659 (Finak et al., 2015). For volcano plots, genes were filtered to show genes with adjusted p-values <0.05  
660 with a >1.2 FC.

661  
662 **Mapping of cells from CS7 gastrula to embryoid bodies**

663  
664 Carnegie stage 7 human gastrula annotations were projected onto our EB dataset based on statistically  
665 enriched proximity in nearest neighbour graphs. Specifically, the aligned datasets were subsetted on the  
666 human CS7 gastrula and EB dataset and used to calculate a KNN graph (using the FindNeighbours  
667 function). For each cell within our EB dataset, the enrichment of individual CS7 gastrula annotations  
668 was calculated using a hypergeometric test, and final annotations assigned based on adjusted p-values.  
669 Cells that showed no significant overlap in KNN graphs were not assigned a lineage.

670  
671 **Mapping of cells to the CS6 marmoset embryo**

672  
673 Cells within our EB were mapped to the marmoset embryo based on proximity in KNN-graphs in the  
674 CCA aligned datasets. Aligned datasets were first subsetted on the marmoset dataset and EB dataset.  
675 For a cell,  $j$ , in the EB dataset, we calculated the KNN from the CS6 embryo, with positions at positions  
676  $\{\mathbf{r}_1, \mathbf{r}_2, \dots, \mathbf{r}_K : \mathbf{r}_i \in \mathbb{R}^3\}$ , and calculated the shared nearest neighbour (SNN) vector  $\boldsymbol{\theta}^{(j)} =$   
677  $\{\theta_1, \theta_2, \dots, \theta_K\}$ . Weights were normalised  $\hat{\boldsymbol{\theta}}^{(j)} = \boldsymbol{\theta}^{(j)}/c$ ,  $c = \sum_i \theta_i$  and a projection of cell  $j$  calculated  
678 as:  $\mathbf{R} = \sum_i \mathbf{r}_i \hat{\theta}_i$ , where  $\mathbf{r}_j \in \mathbb{R}^3$  denotes a 3-dimensional position vector of marmoset cell  $j$ . After  
679 mapping of individual cells, the density of specific groups e.g., PGCLCs (cluster 5 and 6), AMELC  
680 (clusters 7, 9 and 10), basal (cluster 1), was calculated using the MATLAB function mvksdensity.

681  
682 **Doublet detection**

683

684 To minimise doublets in our analyses, we limited the number of cells loaded into each chip, with each  
685 sample capturing around 1000-2000 cells. Potential doublets were identified computationally for each  
686 individual sample using the R package DoubletFinder(McGinnis, Murrow and Gartner, 2019). For  
687 samples with ~1000 captured cells we assumed a doublet rate of 1%, and for samples with ~2000 cells  
688 we assumed a 2% doublet rate. No cluster analysed in this paper was found to contain a high level of  
689 doublets.

690

### 691 **Waddington Optimal Transport analysis**

692

693 Highly variable genes were computed across all single PSCs, PreME and EB cells, and used as input to  
694 PCA, with the first 50 PCs computed using irlba. Cells were assigned to clusters as described above,  
695 which were used as the basis for WOT. Transport maps were computed with parameters ( $\lambda_1=1$ ,  $\lambda_2=50$ ,  
696  $\varepsilon=0.01$ ) between all pairs of time points using the PSCs as 0hours, PreME as 12 hours, and all  
697 subsequent time points as  $12+ti$  for  $i \in \{1, 2, \dots, T\}$  and  $T = \{12, 18, 24, 32, 40, 48, 96\}$ . Ancestor  
698 contributions to populations at subsequent time points were estimated from these transport maps using  
699 the OT trajectory command-line interface (CLI) function. Cell mass contributions between clusters  
700 across time points were concatenated into a cluster:timepoint X cluster:timepoint matrix, where the  
701 rows denote the contribution of clusterj timepointi to clusterj timepointi+1. A power threshold (p=30)  
702 was used to enforce sparsity on this matrix with values  $\leq 0.1$  censored to 0. This sparse matrix was then  
703 used as a weighted adjacency matrix to compute a directed KNN graph ( $k=5$ ), as shown in  
704 Supplementary Figure 6. Meta-clusters were defined on this graph using the Walktrap community  
705 detection algorithm implemented in igraph, which were annotated based on the mean expression level  
706 of single-cells that contribute to each original cluster (Supplementary Figure 6). These annotations were  
707 then mapped back onto the original constituent single-cells based on their cluster identity.

708

### 709 **Acknowledgments**

710

711 M.A.S. was supported by a Wellcome Investigator Awards in Science (209475/Z/17/Z), a MRC –  
712 Research Grant (RG85305) and a BBSRC – Research Grant (G103986). A.C.V. was supported by the  
713 Wellcome 4-Year PhD Programme in Stem Cell Biology and Medicine (203831/Z/16/Z) and the  
714 Cambridge Commonwealth European and International Trust. W.W.C.T. received a Croucher  
715 Postdoctoral Research Fellowship and was supported by the Isaac Newton Trust. T.K. and M.A.S. was  
716 supported by Butterfield Awards of Great Britain Sasakawa Foundation. T.K. was supported by the  
717 Astellas Foundation for Research on Metabolic Disorders. T.E.B. was supported by a Wellcome Sir  
718 Henry Dale Fellowship. Marmoset embryo research is generously supported by the Wellcome Trust  
719 (WT RG89228, WT RG9242), the Centre for Trophoblast Research, the Isaac Newton Trust and JSPS  
720 KAKENHI 15H02360, 19H05759.

721  
722 We would like to thank Roger Barker and Xiaoling He for providing human embryonic tissues, and  
723 Charles Bradshaw for bioinformatic support. We also thank The Weizmann Institute of Science for the  
724 WIS2 hESC line and the Genomics Core Facility of CRUK Cambridge Institute for sequencing services.  
725 We thank members of the Surani lab for insightful comments and critical reading of the manuscript.  
726 J.C.M. acknowledges core support from EMBL and from Cancer Research UK (C9545/A29580), which  
727 supports M.D.M.

728

## 729 **Availability of materials**

730

731 Any enquiries on reagents and cell lines can be directed to (a.surani@gurdon.cam.ac.uk). Plasmids  
732 generated in this study will be made freely available upon request. Modified human embryonic stem  
733 cell lines generated in this study will be made available on request upon completion of a Materials  
734 Transfer Agreement.

735 Single cell RNA-seq (10X) data has been deposited at ArrayExpress under accession numbers E-  
736 MTAB-11283 and E-MTAB-11305. Code for repeating analyses will be available via a GitHub  
737 repository <https://github.com/cap76/PGCLC>.

738

## 739 **Author contributions**

740

741 ACV, CAP, MAS wrote the manuscript with input from all authors. ACV, CAP, MDM designed  
742 experiments and performed analysis. ACV generated human data. SB and ES generated marmoset data.  
743 ACV, WWCT, TK, FCKW performed experiments. MAS, JCM, and TEB supervised.

744

## 745 **References**

746

747 Alberio, R., Kobayashi, T. and Surani, M. A. (2021) ‘Conserved features of non-primate bilaminar disc  
748 embryos and the germline’, *Stem Cell Reports*, 16(5), pp. 1078–1092. doi:  
749 10.1016/j.stemcr.2021.03.011.

750 Angerer, P. *et al.* (2016) ‘destiny: diffusion maps for large-scale single-cell data in R’, *Bioinformatics*,  
751 32(8), pp. 1241–1243. doi: 10.1093/BIOINFORMATICS/BTV715.

752 Bergmann, S. *et al.* (2022) ‘Spatial profiling of early primate gastrulation in utero’, *Nature* 2022, pp.  
753 1–3. doi: 10.1038/s41586-022-04953-1.

754 Bergmann, S. *et al.* (no date) ‘Spatial embryo profiling of primate gastrulation’, *In review*.

755 Bryja, J. and Konečný, A. (2003) ‘Fast sex identification in wild mammals using PCR amplification of  
756 the Sry gene’, *Folia Zoologica*, 52(3), pp. 269–274.

757 Campolo, F. *et al.* (2013) 'Essential role of Sox2 for the establishment and maintenance of the germ  
758 cell line', *Stem Cells*, 31(7), pp. 1408–1421. doi: 10.1002/stem.1392.

759 Chari, T., Banerjee, J. and Pachter, L. (2021) 'The Specious Art of Single-Cell Genomics', *BioRxiv*, pp.  
760 1–25. doi: 10.1101/2021.08.25.457696.

761 Chen, D. *et al.* (2017) 'Germline competency of human embryonic stem cells depends on  
762 eomesodermin', *Biology of Reproduction*, 97(6), pp. 850–861. doi: 10.1093/biolre/iox138.

763 Chen, D. *et al.* (2019) 'Human Primordial Germ Cells Are Specified from Lineage-Primed Progenitors',  
764 *Cell Reports*, 29(13), pp. 4568–4582.e5. doi: 10.1016/j.celrep.2019.11.083.

765 Dobin, A. *et al.* (2013) 'STAR: Ultrafast universal RNA-seq aligner', *Bioinformatics*, 29(1), pp. 15–  
766 21. doi: 10.1093/bioinformatics/bts635.

767 Finak, G. *et al.* (2015) 'MAST: A flexible statistical framework for assessing transcriptional changes  
768 and characterizing heterogeneity in single-cell RNA sequencing data', *Genome Biology*, 16(1), pp. 1–  
769 13. doi: 10.1186/S13059-015-0844-5/FIGURES/6.

770 Gafni, O. *et al.* (2013) 'Derivation of novel human ground state naive pluripotent stem cells', *Nature*,  
771 504(7479), pp. 282–286. doi: 10.1038/nature12745.

772 Guo, F. *et al.* (2015) 'The transcriptome and DNA methylome landscapes of human primordial germ  
773 cells', *Cell*, 161(6), pp. 1437–1452. doi: 10.1016/j.cell.2015.05.015.

774 Guo, G. *et al.* (2020) 'Trophectoderm potency is retained exclusively in human Naïve cells', *bioRxiv*.  
775 doi: 10.1101/2020.02.04.933812.

776 Hirate, Y. *et al.* (2013) 'Polarity-dependent distribution of angiotonin localizes hippo signaling in  
777 preimplantation embryos', *Current Biology*, 23(13), pp. 1181–1194. doi: 10.1016/j.cub.2013.05.014.

778 Hoffman, T. L. *et al.* (2007) 'Tfap2 transcription factors in zebrafish neural crest development and  
779 ectodermal evolution', *Journal of experimental zoology. Part B, Molecular and developmental  
780 evolution*, 308(5), pp. 679–691. doi: 10.1002/JEZ.B.21189.

781 Irie, N. *et al.* (2015) 'SOX17 is a critical specifier of human primordial germ cell fate', *Cell*, 160(1–2),  
782 pp. 253–268. doi: 10.1016/j.cell.2014.12.013.

783 Irie, N., Sybirna, A. and Surani, M. A. (2018) 'What Can Stem Cell Models Tell Us About Human  
784 Germ Cell Biology?', *Current Topics in Developmental Biology*, 129, pp. 25–65. doi:  
785 10.1016/bs.ctdb.2018.02.010.

786 Jo, K. *et al.* (2021) 'Efficient differentiation of human primordial germ cells through geometric control  
787 reveals a key role for NODAL signaling', *bioRxiv*, p. 2021.08.04.455129. doi:  
788 10.1101/2021.08.04.455129.

789 Kanai-Azuma, M. *et al.* (2002) 'Depletion of definitive gut endoderm in Sox17-null mutant mice',  
790 *Development*, 129(10), pp. 2367–2379. doi: 10.1242/dev.129.10.2367.

791 Katoh, Masuko and Katoh, Masaru (2006) 'CER1 is a common target of WNT and NODAL signaling  
792 pathways in human embryonic stem cells', *International Journal of Molecular Medicine*, 17(5), pp.  
793 795–799. doi: 10.3892/IJMM.17.5.795/HTML.

794 Kobayashi, T. *et al.* (2017) 'Principles of early human development and germ cell program from  
795 conserved model systems', *Nature*, 546(7658), pp. 416–420. doi: 10.1038/nature22812.

796 Kobayashi, T. *et al.* (2021) 'Tracing the emergence of primordial germ cells from bilaminar disc rabbit  
797 embryos and pluripotent stem cells', *Cell Reports*, 37(2), p. 109812. doi: 10.1016/j.celrep.2021.109812.

798 Kobayashi, T. and Surani, M. A. (2018) 'On the origin of the human germline', *Development*  
799 (*Cambridge*), 145(16 Special Issue), p. dev150433. doi: 10.1242/dev.150433.

800 Kojima, Y. *et al.* (2017) 'Evolutionarily Distinctive Transcriptional and Signaling Programs Drive  
801 Human Germ Cell Lineage Specification from Pluripotent Stem Cells', *Cell Stem Cell*, 21(4), pp. 517–  
802 532.e5. doi: 10.1016/j.stem.2017.09.005.

803 Kojima, Y. *et al.* (2021) 'GATA transcription factors, SOX17 and TFAP2C, drive the human germ-cell  
804 specification program', *Life Science Alliance*, 4(5). doi: 10.26508/LSA.202000974.

805 Krendl, C. *et al.* (2017) 'GATA2/3-TFAP2A/C transcription factor network couples human pluripotent  
806 stem cell differentiation to trophectoderm with repression of pluripotency', *Proceedings of the National  
807 Academy of Sciences of the United States of America*, 114(45), pp. E9579–E9588. doi:  
808 10.1073/pnas.1708341114.

809 Li, L. *et al.* (2017) 'Single-Cell RNA-Seq Analysis Maps Development of Human Germline Cells and  
810 Gonadal Niche Interactions', *Cell Stem Cell*, 20(6), pp. 858–873.e4. doi: 10.1016/j.stem.2017.03.007.

811 Li, W. and Cornell, R. A. (2007) 'Redundant activities of Tfap2a and Tfap2c are required for neural  
812 crest induction and development of other non-neural ectoderm derivatives in zebrafish embryos',  
813 *Developmental Biology*, 304(1), pp. 338–354. doi: 10.1016/J.YDBIO.2006.12.042.

814 Lin, I. Y. *et al.* (2014) 'Suppression of the SOX2 neural effector gene by PRDM1 promotes human  
815 germ cell fate in embryonic stem cells', *Stem Cell Reports*, 2(2), pp. 189–204. doi:  
816 10.1016/j.stemcr.2013.12.009.

817 Ma, H. *et al.* (2019) 'In vitro culture of cynomolgus monkey embryos beyond early gastrulation',  
818 *Science*, 366(6467). doi: 10.1126/science.aax7890.

819 Martyn, I., Brivanlou, A. H. and Siggia, E. D. (2019) 'A wave of WNT signaling balanced by secreted  
820 inhibitors controls primitive streak formation in micropattern colonies of human embryonic stem cells',  
821 *Development (Cambridge, England)*, 146(6). doi: 10.1242/DEV.172791.

822 McGinnis, C. S., Murrow, L. M. and Gartner, Z. J. (2019) 'DoubletFinder: Doublet Detection in Single-  
823 Cell RNA Sequencing Data Using Artificial Nearest Neighbors', *Cell Systems*, 8(4), pp. 329–337.e4.  
824 doi: 10.1016/J.CELS.2019.03.003/ATTACHMENT/AA430EFF-80F4-471F-8D74-  
825 E3046FA260C8/MMC1.PDF.

826 Minn, K. T. *et al.* (2020) 'High-resolution transcriptional and morphogenetic profiling of cells from  
827 micropatterned human esc gastruloid cultures', *eLife*, 9, pp. 1–34. doi: 10.7554/eLife.59445.

828 Minn, K. T. *et al.* (2021) 'Gene expression dynamics underlying cell fate emergence in 2D  
829 micropatterned human embryonic stem cell gastruloids', *Stem Cell Reports*, 16(5), pp. 1210–1227. doi:  
830 10.1016/j.stemcr.2021.03.031.

831 Moris, N. *et al.* (2020) ‘An in vitro model of early anteroposterior organization during human  
832 development’, *Nature*, 582(7812), pp. 410–415. doi: 10.1038/s41586-020-2383-9.

833 O’Rahilly, R. and Müller, F. (2010) ‘Developmental stages in human embryos: revised and new  
834 measurements’, *Cells, tissues, organs*, 192(2), pp. 73–84. doi: 10.1159/000289817.

835 Pierson Smela, M. *et al.* (2019) ‘Testing the role of SOX15 in human primordial germ cell fate’,  
836 *Wellcome Open Research*, 4, p. 122. doi: 10.12688/wellcomeopenres.15381.2.

837 Rostovskaya, M. *et al.* (2022) ‘Amniogenesis occurs in two independent waves in primates’, *Cell Stem  
838 Cell*, 29(5), pp. 744-759.e6. doi: 10.1016/J.STEM.2022.03.014.

839 Saitou, M., Barton, S. C. and Surani, M. A. (2002) ‘A molecular programme for the specification of  
840 germ cell fate in mice’, *Nature*, 418(6895), pp. 293–300. doi: 10.1038/nature00927.

841 Sasaki, K. *et al.* (2015) ‘Robust In Vitro Induction of Human Germ Cell Fate from Pluripotent Stem  
842 Cells’, *Cell Stem Cell*, 17(2), pp. 178–194. doi: 10.1016/j.stem.2015.06.014.

843 Sasaki, K. *et al.* (2016) ‘The Germ Cell Fate of Cynomolgus Monkeys Is Specified in the Nascent  
844 Amnion’, *Developmental Cell*, 39(2), pp. 169–185. doi: 10.1016/j.devcel.2016.09.007.

845 Schiebinger, G. *et al.* (2019) ‘Optimal-Transport Analysis of Single-Cell Gene Expression Identifies  
846 Developmental Trajectories in Reprogramming’, *Cell*, 176(4), pp. 928-943.e22. doi:  
847 10.1016/j.cell.2019.01.006.

848 Sekiya, T. *et al.* (2004) ‘Identification of BMP and activin membrane-bound inhibitor (BAMBI), an  
849 inhibitor of transforming growth factor-beta signaling, as a target of the beta-catenin pathway in  
850 colorectal tumor cells’, *The Journal of biological chemistry*, 279(8), pp. 6840–6846. doi:  
851 10.1074/JBC.M310876200.

852 Shao, Y., Taniguchi, K., Townshend, R. F., *et al.* (2017) ‘A pluripotent stem cell-based model for post-  
853 implantation human amniotic sac development’, *Nature Communications*, 8(1). doi: 10.1038/s41467-  
854 017-00236-w.

855 Shao, Y., Taniguchi, K., Gurdziel, K., *et al.* (2017) ‘Self-organized amniogenesis by human pluripotent  
856 stem cells in a biomimetic implantation-like niche’, *Nature Materials*, 16(4), pp. 419–427. doi:  
857 10.1038/NMAT4829.

858 Strachan, T., Lindsay, S. (Susan) and Wilson, D. I. (David I. . (1997) ‘Molecular genetics of early  
859 human development’, p. 265.

860 Stuart, T. *et al.* (2019) ‘Comprehensive Integration of Single-Cell Data’, *Cell*, 177(7), pp. 1888-  
861 1902.e21. doi: 10.1016/J.CELL.2019.05.031.

862 Sybirna, A. *et al.* (2020) ‘A critical role of PRDM14 in human primordial germ cell fate revealed by  
863 inducible degrons’, *Nature Communications*, 11(1), pp. 1–18. doi: 10.1038/s41467-020-15042-0.

864 Sybirna, A., Wong, F. C. K. and Surani, M. A. (2019) ‘Genetic basis for primordial germ cells  
865 specification in mouse and human: Conserved and divergent roles of PRDM and SOX transcription  
866 factors’, *Current Topics in Developmental Biology*, 135, pp. 35–89. doi: 10.1016/bs.ctdb.2019.04.004.

867 Tang, W. W. C. *et al.* (2016) ‘Specification and epigenetic programming of the human germ line’,  
868 *Nature Reviews Genetics*, 17(10), pp. 585–600. doi: 10.1038/nrg.2016.88.

869 Tang, W. W. C. *et al.* (2022) ‘Sequential enhancer state remodelling defines human germline  
870 competence and specification’, *Nature Cell Biology*.

871 Teo, A. K. K. *et al.* (2011) ‘Pluripotency factors regulate definitive endoderm specification through  
872 eomesodermin’, *Genes and Development*, 25(3), pp. 238–250. doi: 10.1101/gad.607311.

873 Tyser, R. C. V. *et al.* (2021) ‘Single-cell transcriptomic characterization of a gastrulating human  
874 embryo’, *Nature*, 600(7888), pp. 285–289. doi: 10.1038/s41586-021-04158-y.

875 Vento-Tormo, R. *et al.* (2018) ‘Single-cell reconstruction of the early maternal–fetal interface in  
876 humans’, *Nature*, 563(7731), pp. 347–353. doi: 10.1038/s41586-018-0698-6.

877 Xiang, L. *et al.* (2019) ‘A developmental landscape of 3D-cultured human pre-gastrulation embryos’,  
878 *Nature*, 577(7791), pp. 537–542. doi: 10.1038/s41586-019-1875-y.

879 Yang, R. *et al.* (2021) ‘Amnion signals are essential for mesoderm formation in primates’, *Nature  
880 Communications*, 12(1), pp. 1–14. doi: 10.1038/s41467-021-25186-2.

881 Yu, L. *et al.* (2021) ‘Derivation of Intermediate Pluripotent Stem Cells Amenable to Primordial Germ  
882 Cell Specification’, *Cell Stem Cell*, 28(3), pp. 550–567.e12. doi: 10.1016/J.STEM.2020.11.003.

883 Zhang, J. *et al.* (2018) ‘OTX2 restricts entry to the mouse germline’, *Nature*, 562(7728), pp. 595–599.  
884 doi: 10.1038/s41586-018-0581-5.

885 Zheng, Y. *et al.* (2019) ‘Controlled modelling of human epiblast and amnion development using stem  
886 cells’, *Nature*, 573(7774), pp. 421–425. doi: 10.1038/s41586-019-1535-2.

887 Zhou, F. *et al.* (2019) ‘Reconstituting the transcriptome and DNA methylome landscapes of human  
888 implantation’, *Nature*, 572(7771), pp. 660–664. doi: 10.1038/s41586-019-1500-0.

889 Zhu, Q. *et al.* (2021) ‘Specification and epigenomic resetting of the pig germline exhibit conservation  
890 with the human lineage’, *Cell Reports*, 34(6), p. 108735. doi: 10.1016/j.celrep.2021.108735.

891

892

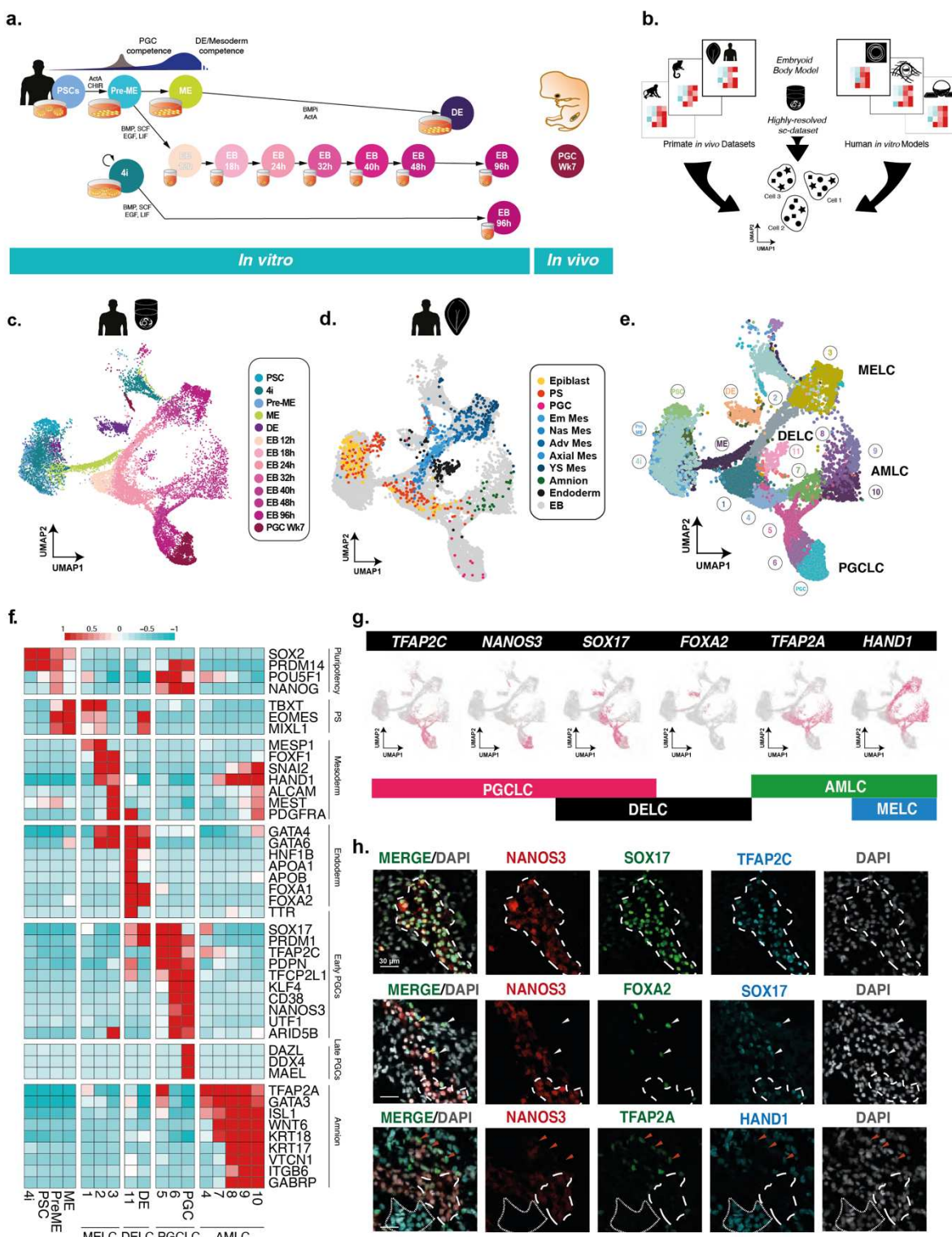
893

894

895

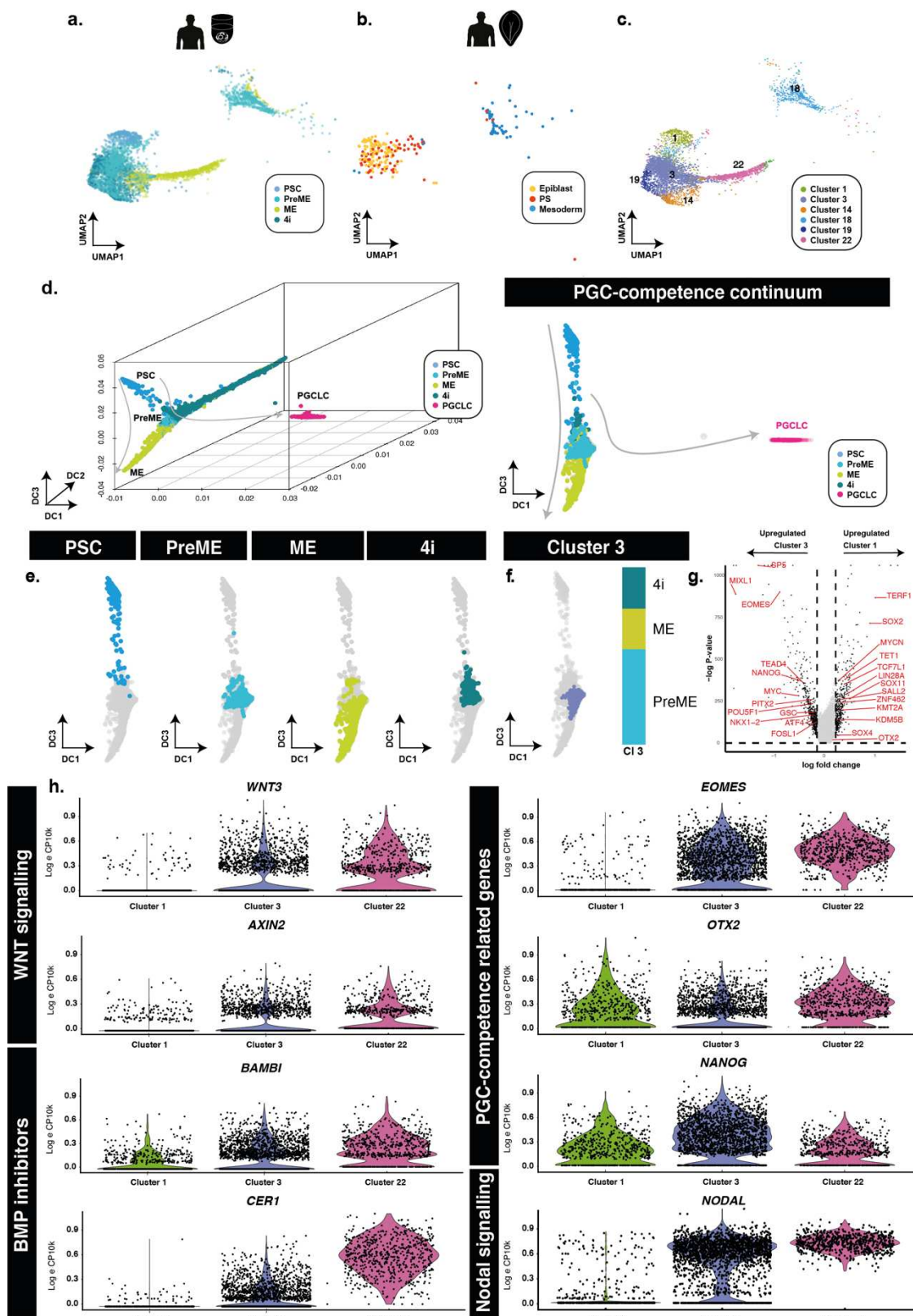
896

897



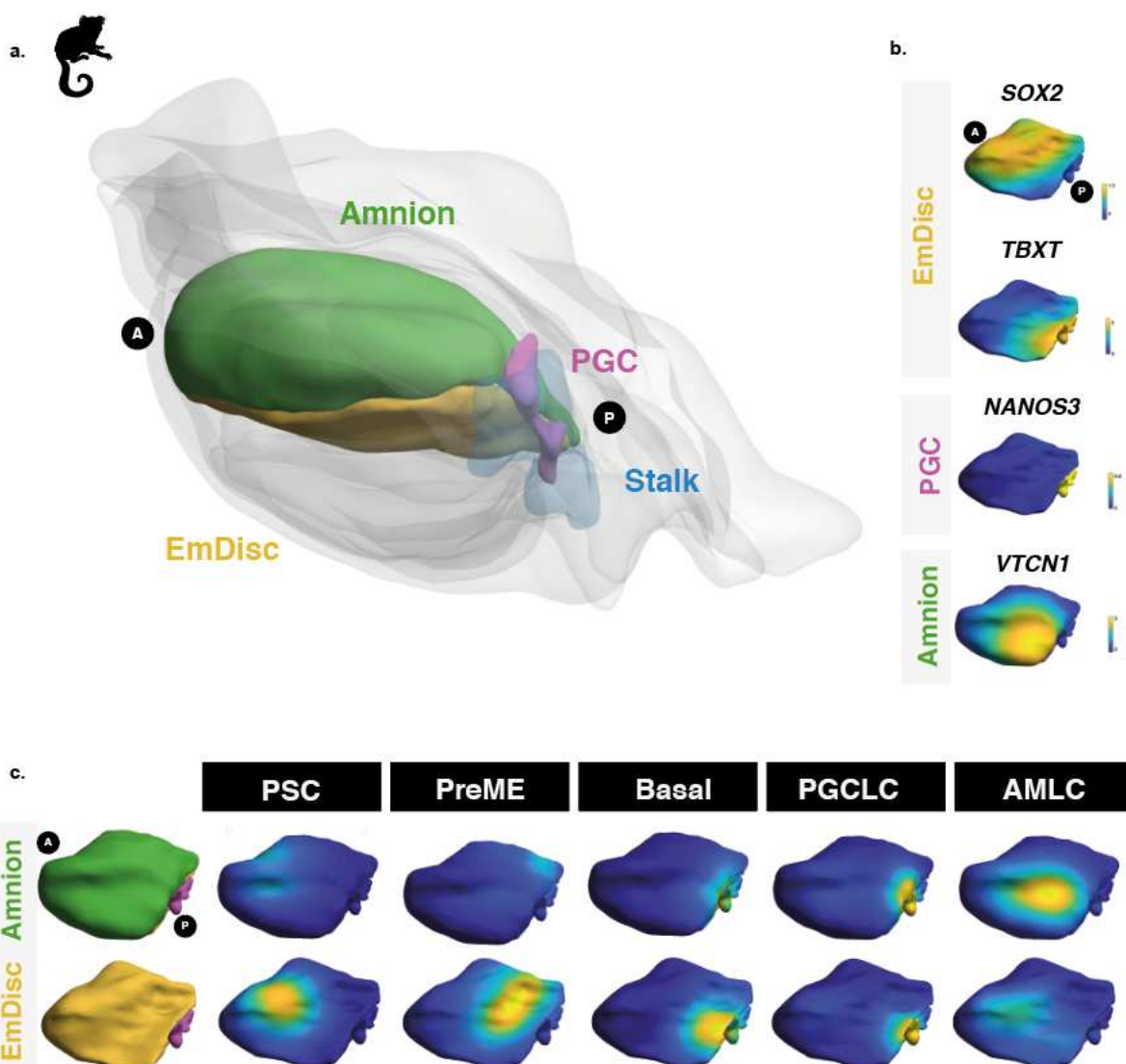
898

899 **Figure 1: A highly resolved roadmap of PGC development and gastrulation.** (a) Experimental design for highly resolved RNA-sequencing  
900 (10X) representing an established PGCLC model, PGCLC-competent populations *in vivo* and *in vitro* reference data. PSC; pluripotent stem  
901 cells, PreME; pre-mesendoderm (transient PGCLC-competent cells), ME; mesendoderm, 4i; four-inhibitor; self-renewing PGCLC-competent  
902 cells, DE; definitive endoderm, PGC; week 7 human gonadal PGCs, EB; embryoid body. (b) Integration of our data with other human *in vitro*  
903 models and primate gastrulation datasets used to generate a roadmap of PGC and early human development. (c) Integrated data representation  
904 as a UMAP projection with samples highlighted by collection time and sample type. (d) Integrated representation of the aligned human CS7  
905 gastrulation data, highlighted by cell type. (e) Louvain clustering of the integrated dataset identified 30 clusters. (f) Heatmaps of pseudobulk  
906 expression for key markers showing that the embryoid body diversifies into mesoderm-like cells (MELC), definitive endoderm-like cells  
907 (DELC), primordial germ cell-like cells (PGCLC), and amnion like cells (AMLC). (g) Combination of key expression markers with TFAP2C,  
908 NANOS3, SOX17 and FOXA2 endoderm fate, and TFAP2A and HAND1 to distinguish mesoderm and amnion fates, respectively. (h) Immunofluorescence of d4 EBs confirms PGCLCs, MELCs, AMLCs, and DELCs.



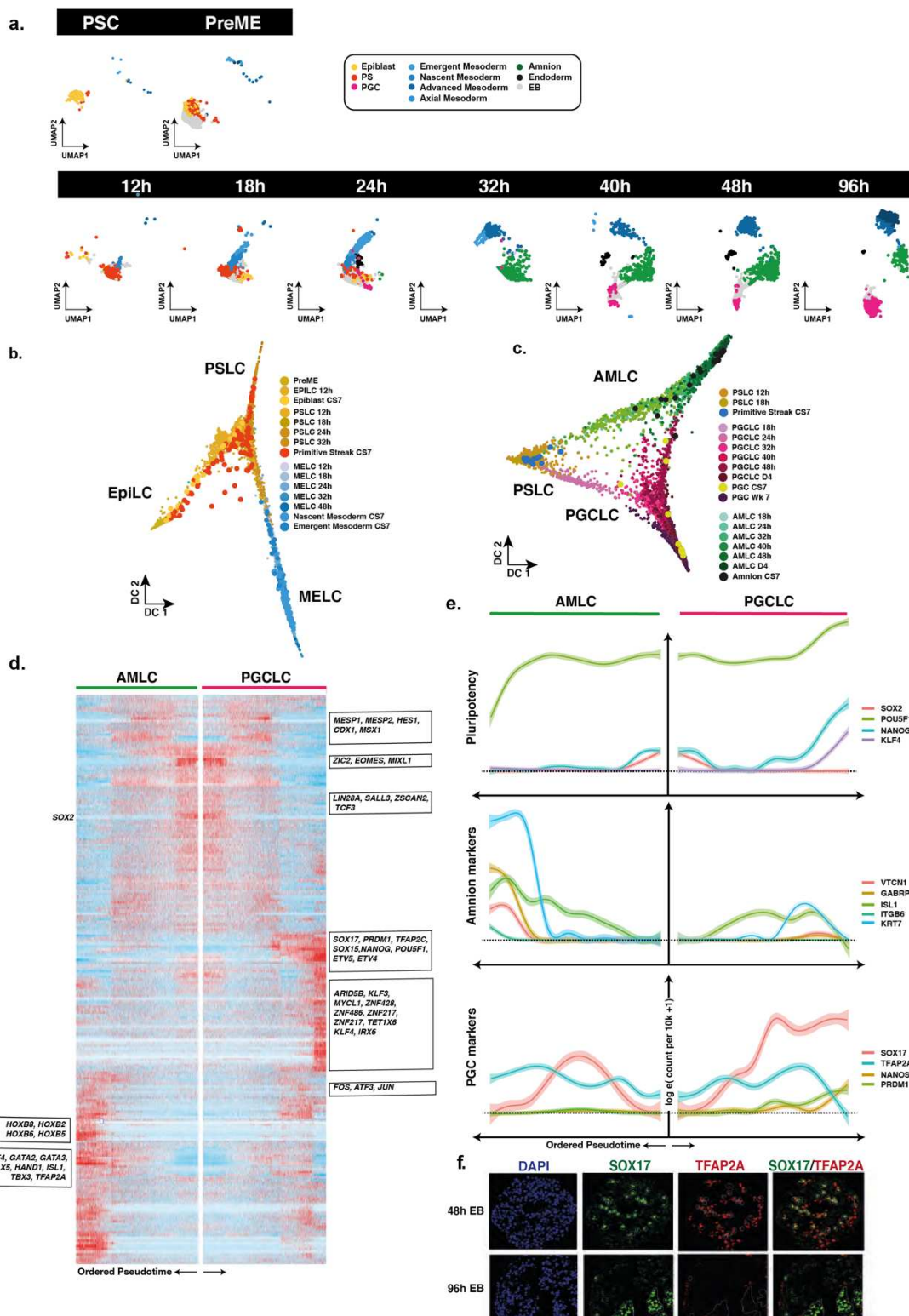
910  
911  
912  
913  
914  
915  
916  
917  
918

**Figure 2: PGCLC competent populations form a continuum of states.** (a) Aligned UMAP representations of pluripotent and PGCLC-competent populations, alongside (b), human *in vivo* samples shows that PSCs align best to pluripotent epiblast cells while competent (PreME and 4i) align to both epiblast-like and primitive-streak-like populations. (c) Sub clustering of competent and non-competent cells identified six main populations; a PSC-dominated \*cluster 1, a mesendoderm-dominated cluster 22, and competence-dominant clusters 3, 14, 19, 22, and 18. (d) Diffusion map representations shows samples lie along a continuum of overlapping states. (e-f) The fractional makeup of competence-dominated subcluster 3 showed almost equal contribution from 4i and PreME cells. (g) Differential expression of competence-dominated subcluster 3 versus PSC-dominant, non-competent subcluster 1 identifies putative regulators of competence. (h) Violin plots of putative competence related genes and markers for WNT and BMP signalling reveal heterogeneous signalling response



919  
920  
921  
922  
923  
924  
925

**Figure 3: Spatial mapping of embryoid body models to gastrulating marmoset embryos reveals posterior bias.** (a) Spatially resolved marmoset embryos at CS6 with the embryonic disc in yellow, amnion in green, PGCs in pink, and stalk in blue. Extraembryonic tissues are shown in grey. (b) Expression analysis in the marmoset embryo shows the anterior embryonic disc is *SOX2* and the posterior, T positive, respectively. Specified PGCs with *NANOS3* expression, amnion with partial *VTCN1* expression. (c) Mapping *in vitro* cells shows PSCs map best to the anterior embryonic disc. Competent populations show a distinct posterior bias, with PGCLCs showing strong localisation to posterior-most PGC region and AMLCs mapping to the amnion.



926

927

928  
929

929  
930

931  
032

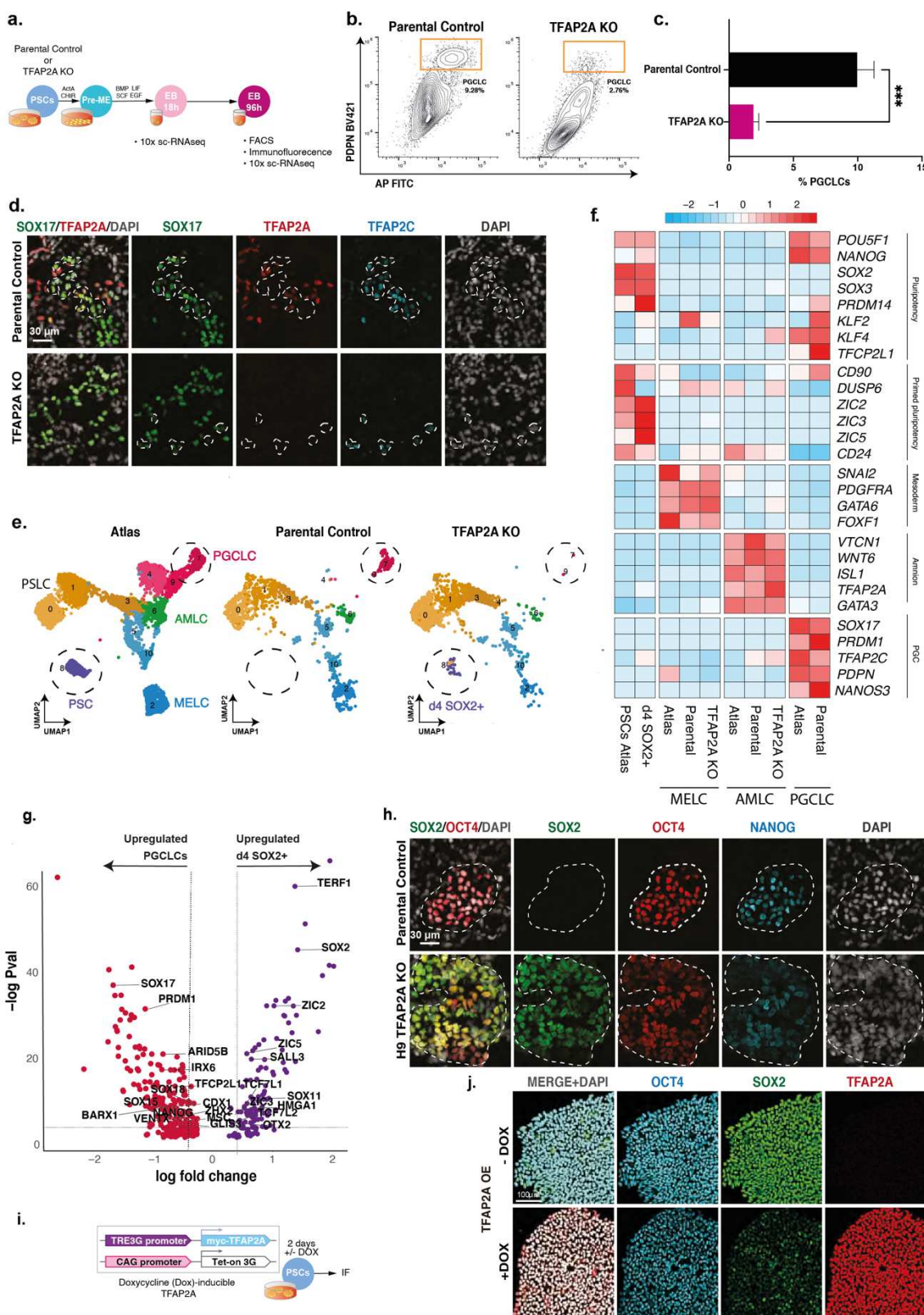
932  
933

934  
025

935  
936

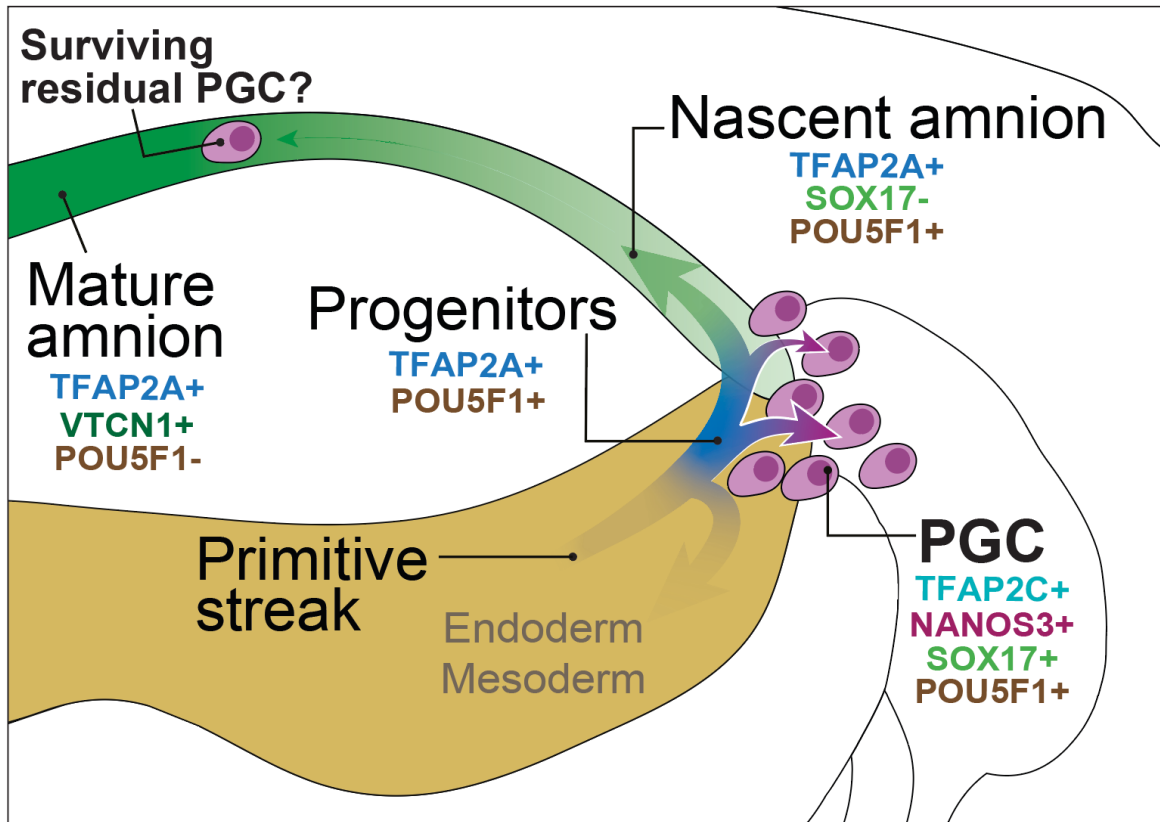
2

**Figure 4: Resolving the dynamics of bifurcations in embryoid bodies.** (a) Visualisation of data separated by sample time with cells annotated by transfer of labels from the human CS7 gastrula<sup>1</sup>; representation suggests EBs develops first through a primitive streak-like stage, early emergence of mesoderm-like cells and primordial germ cell-like cells, followed by amnion-like cells. (b) Diffusion map representation of specific clusters reveals strong bifurcation of mesoderm from the PS-like progenitors, with the remaining PS-like cells destined for other lineages. (c) Diffusion map representation of AMLC and PGCLCs shows bifurcation from common progenitor cells, with the continued association until 48h. Superimposition of cells from the CS7 gastrula labelled as PS, amnion or PGCs shows early alignment of hPGCs to PGCLCs. (d) WOT analysis to infer progenitor-descendent relationships, identifying bifurcations of individual lineages. Heatmap representants differentially expressed genes between AMLC and PGCLC ordered by pseudotime. (e) Line plot representations of essential genes ordered by pseudotime shows early up-regulation of TFAP2A in both PGCLC and AMLCs, which is sustained in AMLC. (f) IF shows TFAP2A in early PGCLCs at 48h (SOX17/TFAP2A double-positive) is lost by 96h.



937  
938  
939  
940  
941  
942  
943  
944  
945

**Figure 5: TFAP2A is a regulator of PGCLC fate.** (a) Testing the role of TFAP2A in PGC specification. (b) FACS plot reveals % PGCLCs in TFAP2A KO EBs and WT parental control. (c) Immunofluorescence shows co-expression for SOX17, TFAP2A and TFAP2C in d4 EB. (d) Quantification of PGCLC (%) in WT and TFAP2A KO. (e) Aligned UMAPs for the reference data versus parental control and H9 TFAP2A KO. (f) Row-normalised gene expression demonstrate consistent expression in AMLC and MELC in the TFAP2A KO line. D4 SOX2+ cells shows expression of pluripotency genes. (g) Immunofluorescence of d4 parental EBs shows OCT4 NANOG double-positive cells (PGCLCs) but not in TFAP2A KO EBs; instead, there are OCT4, NANOG, and SOX2 triple positive cells. (h) Volcano plot for differentially expressed genes between the d4 SOX2+ cluster in TFAP2A KO vs PGCLCs in parental control (i) Testing the role of TFAP2A overexpression in PSCs. (j) Immunofluorescence for OCT4, SOX2, TFAP2A in PSCs.



946  
947  
948  
949  
950

**Figure 6: A unifying model of PGC specification in bilaminar disc embryos.** PGCs are specified from *TFAP2A*-positive progenitors at the posterior end of the embryonic disc, which also give rise to nascent amnion. PGCs in the amnion specified at an earlier stage might only contribute to the founder PGC pool if they can migrate against the flow of nascent amnion expansion.